

Test of Basic Properties for Radiation Damage  
Measurement of Silicon Detector for the ILD  
Electro-magnetic Calorimeter

Chihiro Kozakai

Department of Physics, Graduate School of Science, The University of Tokyo

2014/2/5



## Abstract

A silicon tungsten sampling sandwich calorimeter is being developed for the ILD, one of the detector concepts for the ILC. The development of a high granularity electro-magnetic calorimeter is required for Particle Flow Algorithm. Silicon detector allows high granularity multi channel readout without much difficulty. Therefore, detectors using silicon semiconductor can be important technology not only for the ILD electro-magnetic calorimeter but also for other future collider experiments. Since the use of the silicon detector will be under severe radiation in the years ahead, radiation hardness of the sensor and the glue for the sensor and readout electronics is concerned. In this thesis, it is discussed how to evaluate the radiation damage from measurements of the current-voltage properties, the capacitance-voltage properties, and the charge collection efficiency measurement to extract the change of the dependence of the leakage current on temperature, carrier concentration change, and charge collection deficiency after irradiation.



# Contents

<b>1</b>	<b>Introduction</b>	<b>7</b>
1.1	International Linear Collider . . . . .	7
1.2	International Large Detector . . . . .	9
1.3	Particle Flow Algorithm (PFA) . . . . .	9
1.4	SiW electromagnetic calorimeter . . . . .	14
1.5	Overview . . . . .	15
<b>2</b>	<b>Silicon sensor basic properties</b>	<b>17</b>
2.1	The design of silicon sensor for the ILD ECAL . . . . .	17
2.2	Silicon sensor properties . . . . .	17
2.2.1	The PIN diode property . . . . .	17
2.2.2	Current-voltage property . . . . .	22
2.2.3	Capacitance-voltage property . . . . .	26
2.2.4	Signal collection . . . . .	31
2.3	Expected effects by radiation exposure . . . . .	31
2.4	The requirement for silicon sensor for the ILD ECAL . . . . .	34
<b>3</b>	<b>Current-voltage measurement</b>	<b>35</b>
3.1	Setup . . . . .	35
3.2	Leakage current . . . . .	38
3.3	Temperature dependence . . . . .	42
<b>4</b>	<b>Capacitance-voltage measurement</b>	<b>45</b>
4.1	Setup . . . . .	45
4.2	Systematic error estimation study . . . . .	48
4.3	Depletion width, diffusion voltage . . . . .	51
<b>5</b>	<b>Charge collection efficiency measurement plan</b>	<b>55</b>
5.1	Expected signal voltage . . . . .	55
5.2	Setup . . . . .	55

<b>6</b>	<b>Simulation of radiation damage effect</b>	<b>59</b>
6.1	Simulation tools . . . . .	59
6.2	Result . . . . .	59
6.3	The requirements on the silicon sensor . . . . .	61
<b>7</b>	<b>Irradiation experiment plan</b>	<b>65</b>
7.1	Radiation dose . . . . .	65
7.2	Irradiation experiment . . . . .	67
<b>8</b>	<b>Conclusion</b>	<b>69</b>
<b>9</b>	<b>Acknowledgements</b>	<b>71</b>
<b>A</b>	<b>NIEL</b>	<b>73</b>
<b>B</b>	<b>The Keithley2410 high-voltage source meter specification</b>	<b>75</b>
<b>C</b>	<b>The Agilent LCR meter specification</b>	<b>77</b>

# Chapter 1

## Introduction

### 1.1 International Linear Collider

The International Linear Collider (ILC) is a future electron-positron collider operating at centre-of-mass energies between 250 GeV and 1 TeV [1][2]. The schematic layout of the ILC is shown in Fig.1.1. It is a multi purpose experiment. One of the main physics targets at the ILC is the precise measurement of the Higgs boson couplings. After the discovery of Higgs boson at the LHC in July 2012, the measurement of Higgs couplings is very important probe to test the Standard Model and to open the way to new physics. Higgs couplings can be measured with less than percent order precision with the ILC and the deviations from the Standard Model can be crucially tested. In addition to Higgs boson physics, broad topics in elementary particle physics such as top quark, W boson, Z boson and new physics such as supersymmetry can be investigated with the ILC.

The physics advantage of the ILC is that the elementary electroweak coupling  $e$  of the photon is the same for all species of quarks and leptons, and the same also for new particles from beyond the Standard Model. It leads to comparable cross sections of beyond the Standard Model particles to those of the Standard Model backgrounds. At the LHC, the gluon couples to all the quarks and new coloured particles. However, soft, non-perturbative strong interactions are dominant mechanism for particle production and involve only light quarks and gluons. Further, because the proton is a composite object with parton energy distributions that fall steeply with its energy fraction, the production cross sections are much lower for heavy particles than for light particles. Thus, only events with unusual and striking properties can be recognized against the much larger samples of background QCD events. At the ILC, since the production cross section of new particle is comparable to the Standard Model background, new particle production events are clearly distinguishable from the Standard Model reactions.

Moreover, because initial state  $e^+$  and  $e^-$  are point-like elementary particles, coupling only via the electroweak interactions, theoretical cross sections can be calculated with parts-per-

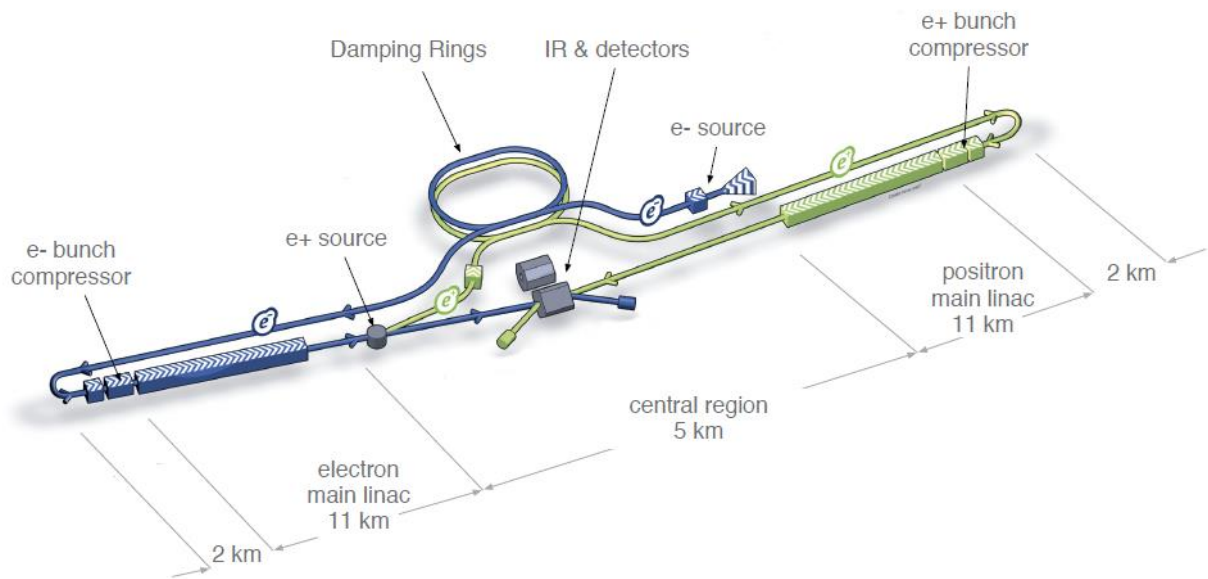


Figure 1.1: Schematic layout of the ILC, indicating all the major subsystems. [1]

mil level precision. The ILC can also provide polarized beams, allowing the spin-dependence of production and decay rate to be revealed. It also gives interesting events efficiently with polarized beams.

The advantage of the ILC from the point of view of detector design is very low chronic background from photon-photon collision. This means low occupancy rate and loose radiation hardness requirement compared to the LHC. Therefore, the vertex detector can be placed much closer to the interaction point and they can achieve high precision measurement. The ILC can record all events, with no trigger needed.

## 1.2 International Large Detector

There are two detector designs for the ILC. One of the detectors at the ILC interaction point is called the ILD (International Large Detector). Fig.1.2, 1.3 shows a view of the ILD concept. For physics at the ILC, many important channels have multi jet final states. Therefore, high jet energy resolution is required for the detector.

From innermost region, the ILD consists of a pixel vertex detector, silicon strip detectors, time projection chamber, further silicon strip detectors, electromagnetic calorimeter (ECAL), hadronic calorimeter (HCAL), superconducting solenoid and iron return yoke. In addition, a system of two silicon-pixel disks and five silicon-strip disks (FTD), and radiation hard calorimetric detectors (LumiCAL, BeamCAL, LHCAL) are placed in the very forward region. The ILD detector is optimised for Particle Flow Algorithm (PFA), described in the next section.

## 1.3 Particle Flow Algorithm (PFA)

The required precision is 3-4 % for 100 GeV jets. This is a requirement to distinguish W and Z di-jet final state. Particle Flow Algorithm (PFA) for jet energy reconstruction have been developed to meet this requirement [3]. The basic idea of the PFA is that each particle should be measured with the most appropriate detectors. The energy of electrons and hadrons can be measured with calorimeter. However, for charged particles up to 200 GeV transverse momentum, the tracker measures energy with better resolution than the calorimeter in the ILD. If it is distinguished that whether a cluster in a calorimeter was produced by a charged particle or a neutral particle, PFA is achieved. One simulated PFA reconstruction result is shown in Fig.1.4.

This enables the required precision of 3-4 % for 100 GeV jets to be achieved, the requirement to separate W and Z di-jet final states. Fig.1.5 shows the distribution of reconstructed mass of two W bosons or two Z bosons. These plots are based on the best jet-pairing in selected  $\nu_e\bar{\nu}_e$  WW (blue) and  $\nu_e\bar{\nu}_e$  ZZ (red) events at  $\sqrt{s} = 1$  TeV.

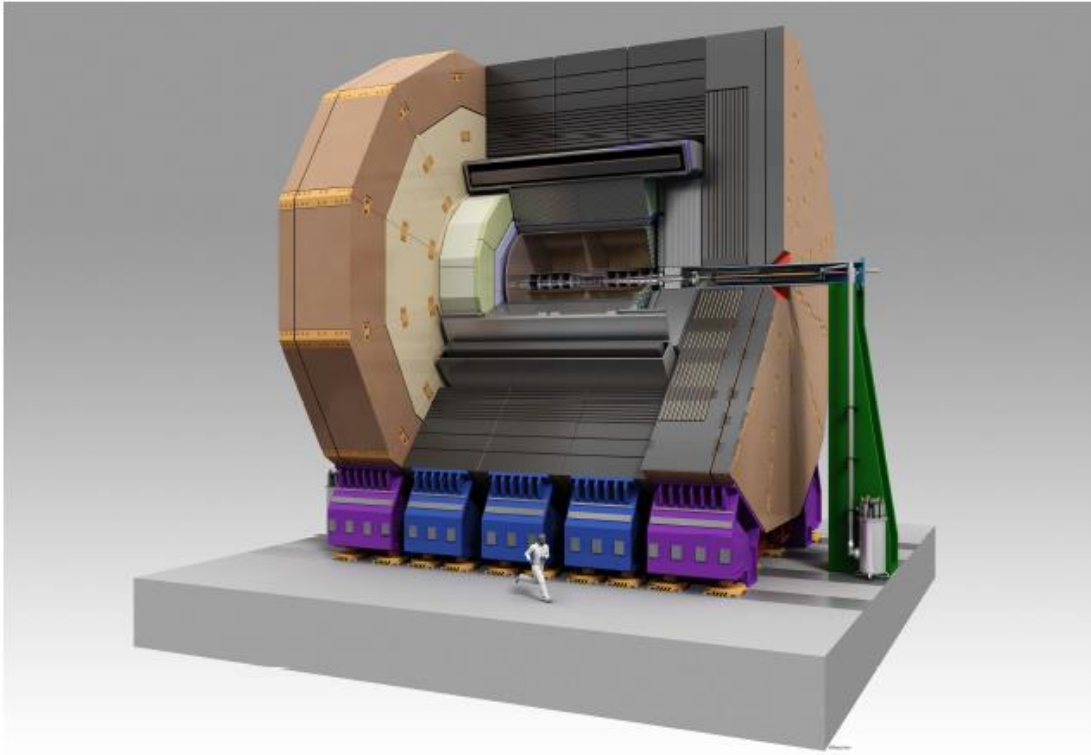


Figure 1.2: View of the ILD concept. [1]

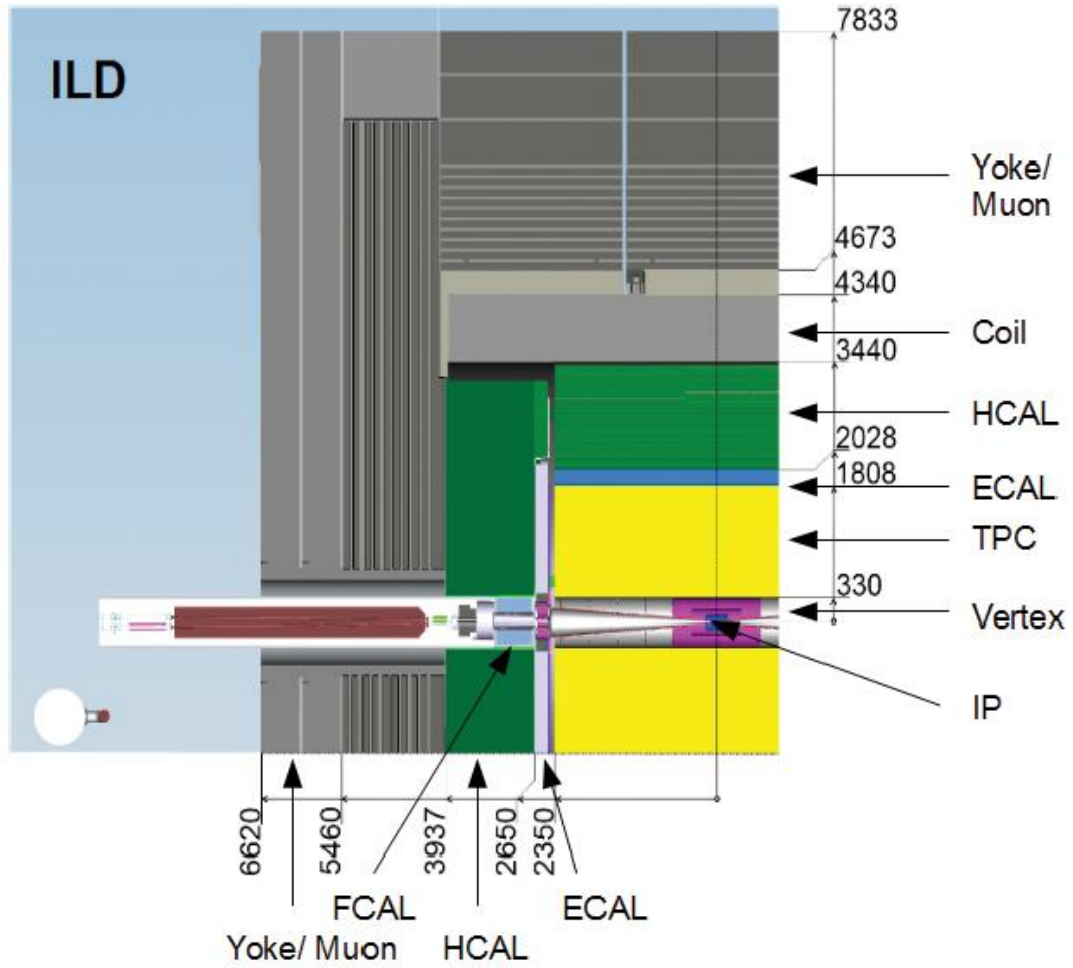


Figure 1.3: Quadrant view of the ILD concept. [1]

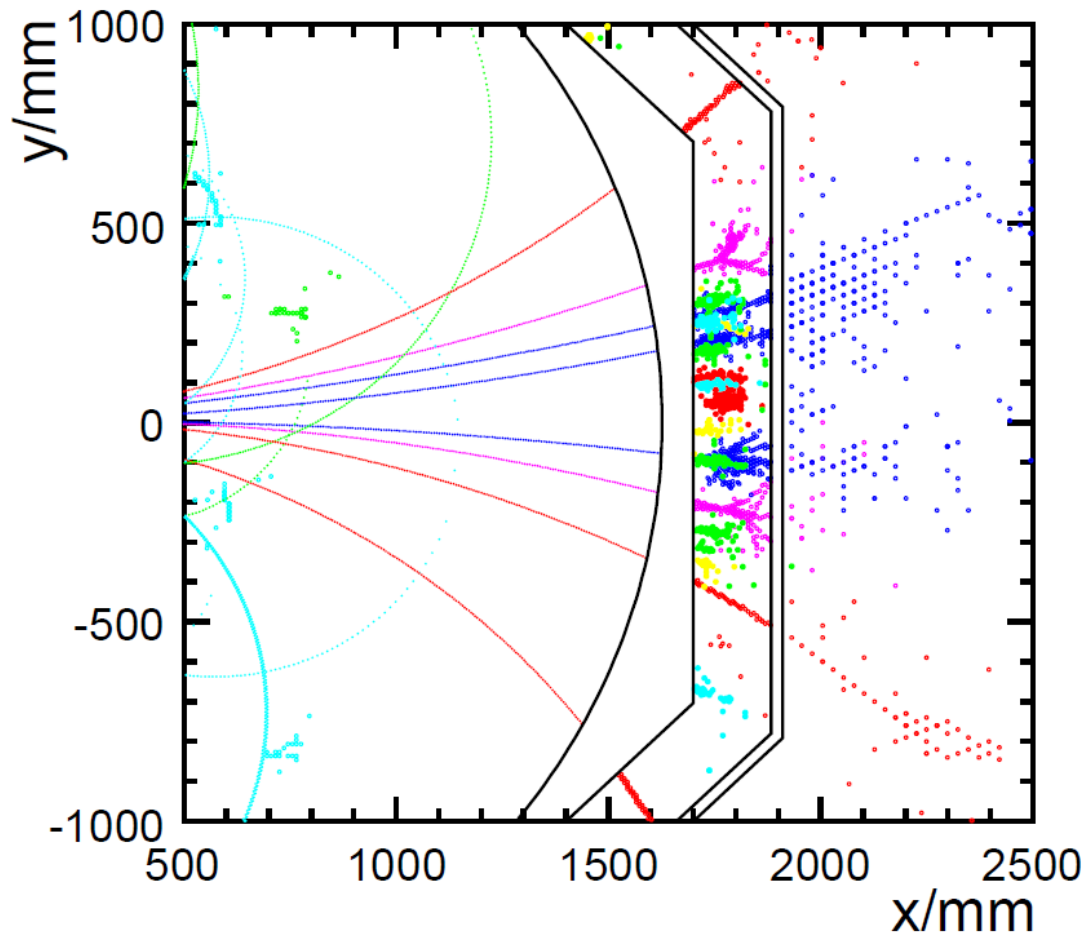


Figure 1.4: Simulation of a 100 GeV jet reconstructed by PFA. [3]

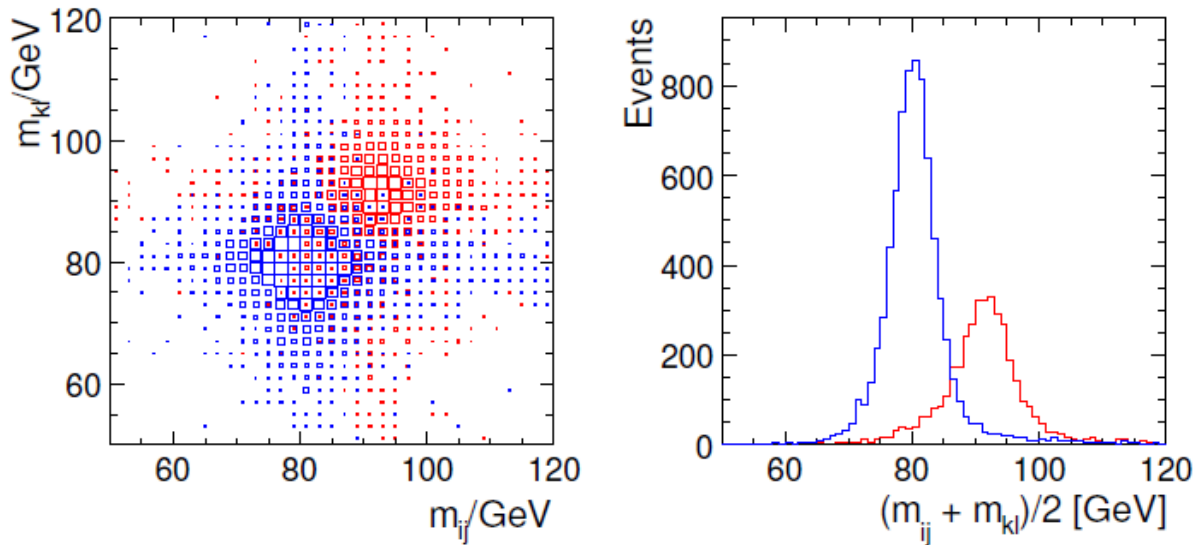


Figure 1.5: a) The reconstructed di-jet mass distributions for the best jet-pairing in selected  $\nu_e\bar{\nu}_e$  WW (blue) and  $\nu_e\bar{\nu}_e$  ZZ (red) events at  $\sqrt{s} = 1$  TeV. b) The distribution of the average reconstructed di-jet mass,  $(m_{ij} + m_{kl}^B)/2.0$ , for the best jet-pairing for  $\nu_e\bar{\nu}_e$  WW (blue) and  $\nu_e\bar{\nu}_e$  ZZ (red) events. [2]

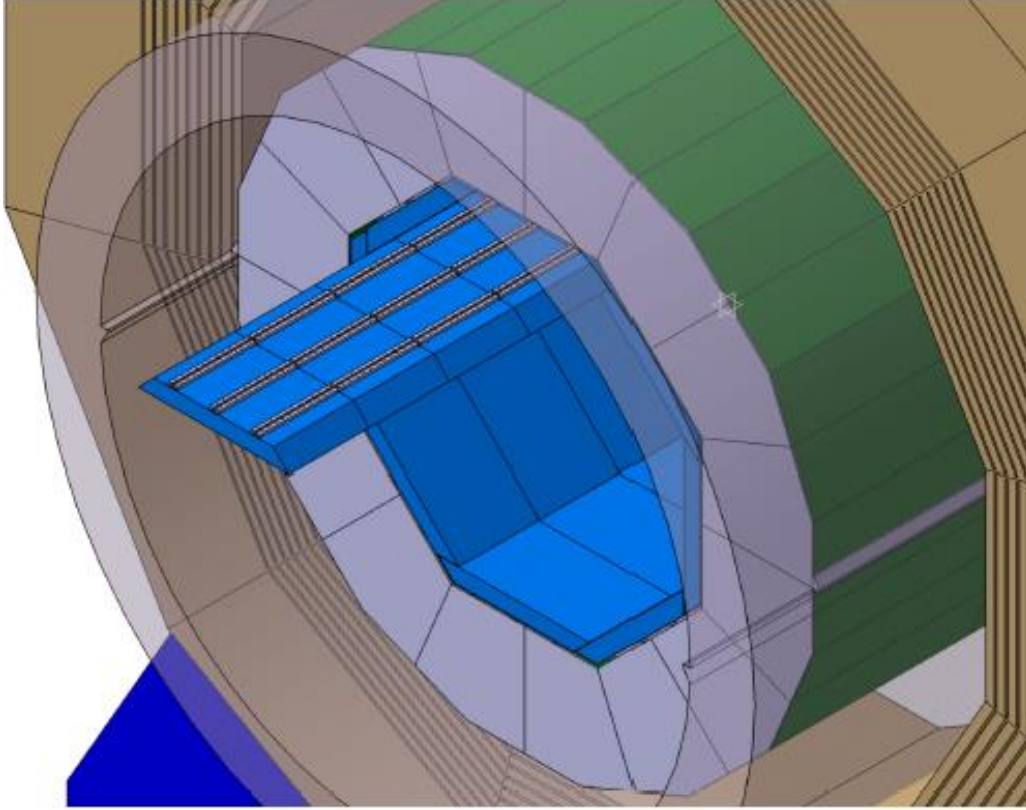


Figure 1.6: The barrel region of the electromagnetic calorimeter (blue) within the ILD detector.[1]

## 1.4 SiW electromagnetic calorimeter

The ECAL is one of the most challenging detectors in the ILD for PFA requirements. The SiW ECAL is an option for it. SiW ECAL is a sandwich-type calorimeter with layers of tungsten absorbers and silicon semiconductor detectors. Fig.1.6 shows a picture of the barrel region of the ECAL within the ILD. For PFA requirements, each particle cluster in a ECAL should be separated. Tungsten absorber is the best for this purpose. It is because the tungsten has a short radiation length ( $X_0 = 3.5$  mm), small Moliere radius ( $R_M = 9$  mm), and large interaction length to radiation length ratio. These properties lead to compact electromagnetic showers and make it easier to distinguish electromagnetic showers from hadronic showers. The silicon detector layer has high granularity. The segmentation is  $5 \times 5$  mm<sup>2</sup> in the current design. The ECAL is longitudinally segmented into 30 layers.

## 1.5 Overview

This paper describes tests of basic properties of silicon sensors being developed for the SiW ECAL of the ILD. This is for understanding the sensor's behaviour and for future radiation damage measurement of the silicon sensor.

The physics of the silicon semiconductor detector and radiation effects will be described in chapter 2. Then the measurement of each property will be shown in chapters 3-5. In chapter 6, some effects of radiation damage on the ILD performance are investigated using the ILD full simulation. A plan for a future irradiation experiment is presented in chapter 7.



# Chapter 2

## Silicon sensor basic properties

### 2.1 The design of silicon sensor for the ILD ECAL

The silicon semiconductor detector for the ILD ECAL, shown in Fig.2.1, is a matrix of PIN diode.

The size is  $8.97 \times 8.97 \text{ cm}^2$ . It has  $16 \times 16$  pixels. The schematic diagram of the silicon sensor for thickness direction is shown in Fig.2.2. The thickness is  $350 \mu\text{m}$ , including electrode metal and insulator. The silicon thickness itself is  $320 \pm 15 \mu\text{m}$ . The p-type layer has a segmentation of  $5.50 \times 5.50 \text{ mm}^2$ . Thus it gives higher position precision than Molière radius. It is surrounded by 0.5 mm wide guard ring to suppress the surface current and thus keep dynamic range of readout electronics.

Chips with  $3 \times 3$  pixels, called baby chips, have also been produced from the same wafer as the chip noted above for testing of different guard ring designs. The size of the baby chip is  $1.75 \times 1.75 \text{ cm}^2$ .

The results shown in this paper are for a main chip and 3 baby chips with same guard ring design as main chip. The baby chips will be used for radiation hardness tests.

### 2.2 Silicon sensor properties

#### 2.2.1 The PIN diode property

Here, it will be described how the silicon sensor works. This section describes the PIN diode physics applying the discussion in [4] about pn diode. In the semiconductor diode, p-type semiconductor which is doped with acceptor has holes and n-type one which is doped with donor has free electrons. Undoped semiconductor, intrinsic layer has few holes and free electrons. The PIN diode is consists of p-type layer, intrinsic layer, and n-type layer. The intrinsic layer is sandwiched between p-type layer and n-type layer. When a forward bias voltage (p-type layer is higher side) is applied, the current becomes large because the

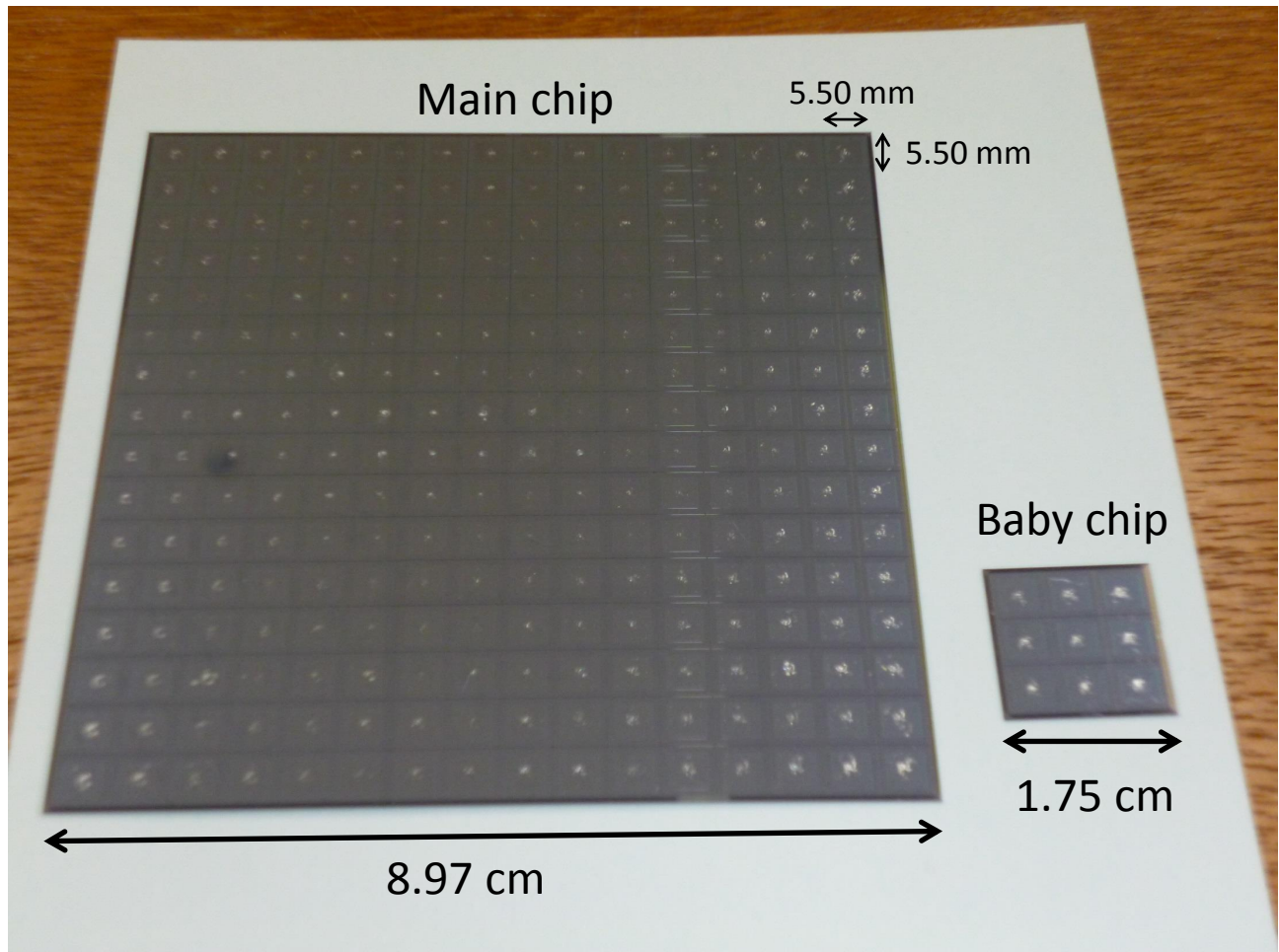


Figure 2.1: A silicon sensor main chip for the ILD ECAL and a baby chip.

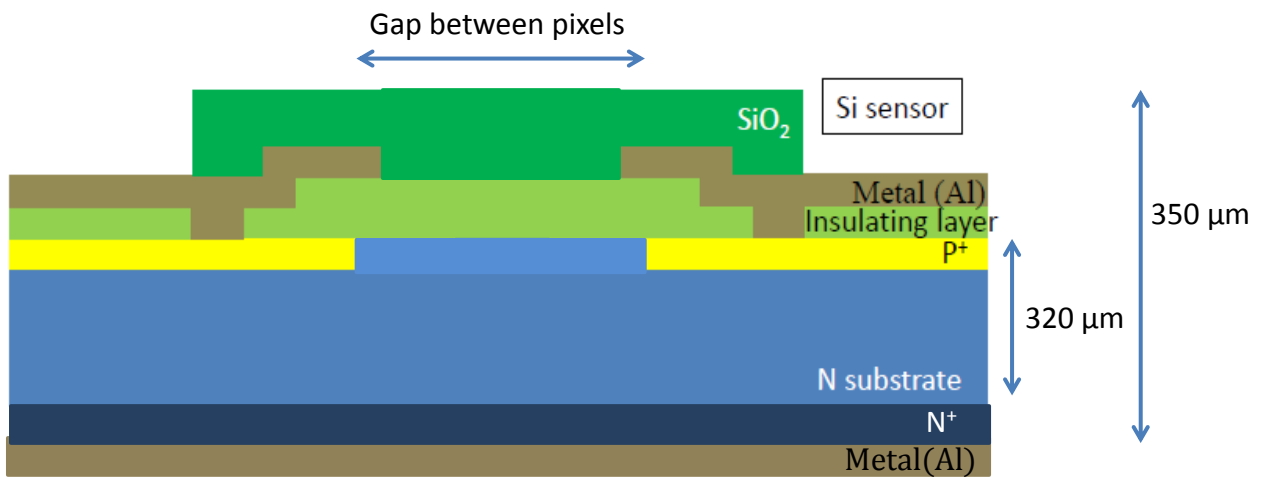


Figure 2.2: A schematic diagram of the silicon sensor for thickness direction.

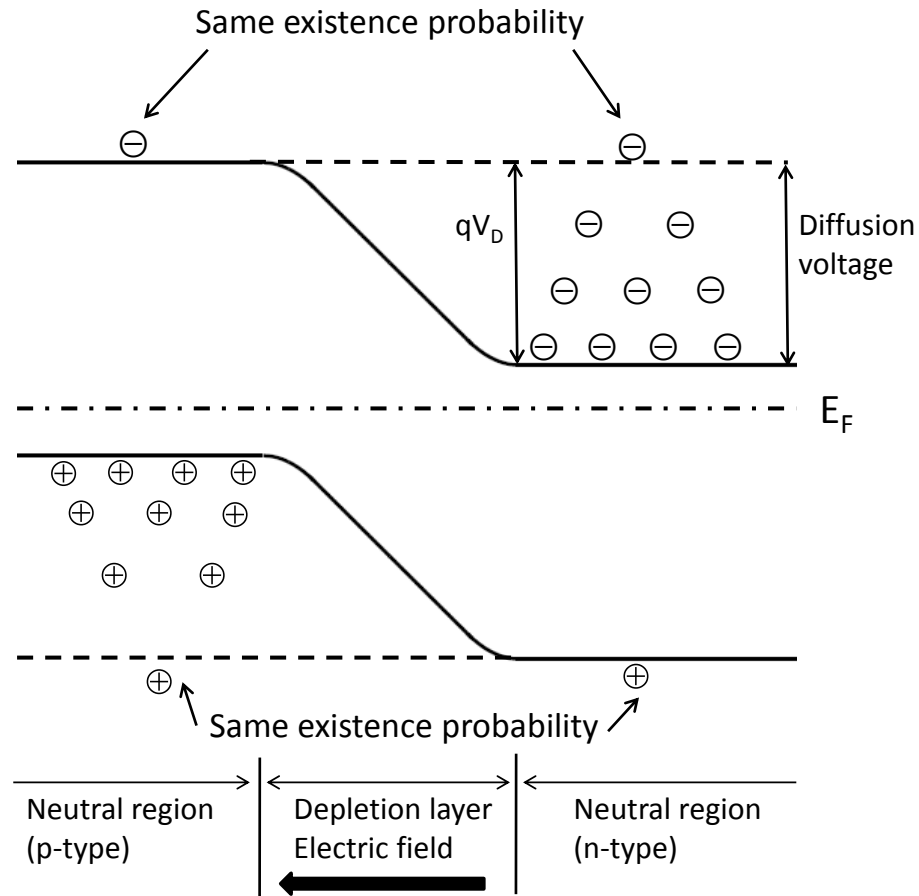


Figure 2.3: An energy band chart for a PIN diode.

potential barrier between p-type and n-type becomes small. However, when a reverse bias voltage (n-type layer is higher side) is applied, current becomes significantly small because carriers move to each electrode and disappear from the semiconductor. In this case, there is a volume with few carriers and fully ionized donors (or acceptors) out of the intrinsic layer. This is called the depletion layer including intrinsic layer. An electric field exists only in the depletion layer. Here, the voltage direction is defined to be positive when p-type layer is the higher side.

The energy band chart is introduced for a description. Fig.2.3 is an energy band chart for a PIN diode. The left side is p-type and the right side is n-type. The central region is the depletion layer. The upper curve shows the bottom of the conduction band ( $E_C$ ) and the lower curve shows the top of the valence band ( $E_V$ ). The broken line at the centre is the Fermi level ( $E_F$ ).

The energy difference between the bottom of the p-type and the n-type conducting bands

at equilibrium is defined as  $qV_D$ .  $V_D$  is called the diffusion voltage. Equilibrium is reached when the Fermi levels in the n-type and the p-type regions are equal.

The diffusion voltage  $V_D$  is derived below. The electron carrier concentration  $n$  can be represented as

$$n = N_C f_B(E_C) \quad (2.1)$$

$$N_C \equiv 2 \left( \frac{2\pi m_e^* kT}{h^2} \right)^{3/2} \quad (2.2)$$

$$f_B(E_C) \equiv e^{-(E_C - E_F)/kT} \quad (2.3)$$

Here,  $m_e^*$  is the effective electron mass in silicon.  $N_C$  is called the effective density of states.  $f_B(E_C)$  is the value of the Maxwell-Boltzmann distribution at  $E = E_C$ . The effective density of states for the hole concentration,  $p$ , is similarly

$$p = N_V \{1 - f(E_V)\} = N_V e^{-(E_F - E_V)/kT} \quad (2.4)$$

$$N_V \equiv 2 \left( \frac{2\pi m_h^* kT}{h^2} \right)^{3/2} \quad (2.5)$$

$$f(E_V) \equiv \frac{1}{1 + e^{-(E_F - E_V)/kT}} \simeq 1 - e^{-(E_F - E_V)/kT} \quad (2.6)$$

From (2.1) and (2.4),

$$pn = N_C N_V e^{-(E_C - E_V)/kT} \quad (2.7)$$

For an intrinsic, undoped semiconductor,  $n = p = n_i$  and  $pn = n_i^2$ . This  $n_i$  is called the intrinsic carrier concentration.

This depends only on the temperature  $T$  and the band gap  $E_C - E_V$ .  $E_C$  is different in the p-type and the n-type regions. Therefore,

$$n_n = N_C e^{-(E_{Cn} - E_F)/kT} \quad (2.8)$$

$$n_p = N_C e^{-(E_{Cp} - E_F)/kT} \quad (2.9)$$

Therefore,

$$qV_D = E_{Cp} - E_{Cn} = kT \ln \frac{n_n}{n_p} \quad (2.10)$$

At room temperature, most of donors and acceptors are ionized. Therefore, the free electron concentration nearly equals to  $N_D$ , donor concentration in n-type layer, and the hole concentration nearly equals to  $N_A$ , acceptor concentration in p-type layer. Using  $pn = n_i^2$ ,

$$n_n \simeq N_D \quad (2.11)$$

$$n_p \simeq n_i^2/N_A \quad (2.12)$$

Here,  $N_D$  is the donor concentration in the n-type layer and  $N_A$  is the acceptor concentration in the p-type layer. Substituting (2.11) and (2.12) into (2.10),

$$V_D = \frac{kT}{q} \ln \frac{N_A N_D}{n_i^2} \quad (2.13)$$

Thus, the diffusion voltage  $V_D$  depends on the impurity concentration,  $N_A$  and  $N_D$ .

### 2.2.2 Current-voltage property

If a reverse bias voltage is applied to the silicon sensor, most of the bias voltage goes to the depletion layer because the depletion layer has a high resistance due to a low carrier concentration. Here, the voltage difference between the Fermi levels of the p-type and the n-type is equal to the applied reverse bias voltage. The energy barrier becomes  $q(V_D + V)$ . The energy band chart is shown in Fig.2.4.

To go over the energy barrier, the electron must have energy larger than  $q(V_D + V)$ . If the energy distribution can be approximated by the Maxwell-Boltzmann distribution, the current density moving from n-type side to p-type side can be written as

$$I_{np} = K_1 e^{-q(V_D+V)/kT} \quad (2.14)$$

Here,  $K_1$  is a constant and independent on the bias voltage.

For an electron moving from the p-type side to the n-type side, the energy barrier doesn't matter. Therefore, if the number of electrons moving from p-type side to n-type side per unit area per unit time is  $I_{pn}$ ,

$$I_{pn} = K_2 \quad (2.15)$$

Here,  $K_2$  is a constant and independent on the bias voltage. The total electron current density  $J_e$  is then

$$J_e = -q(I_{np} - I_{pn}) = -q(K_1 e^{-q(V_D+V)/kT} - K_2). \quad (2.16)$$

Because  $J_e = 0$  at  $V = 0$ ,

$$K_2 = K_1 e^{-qV_D/kT} \quad (2.17)$$

Therefore

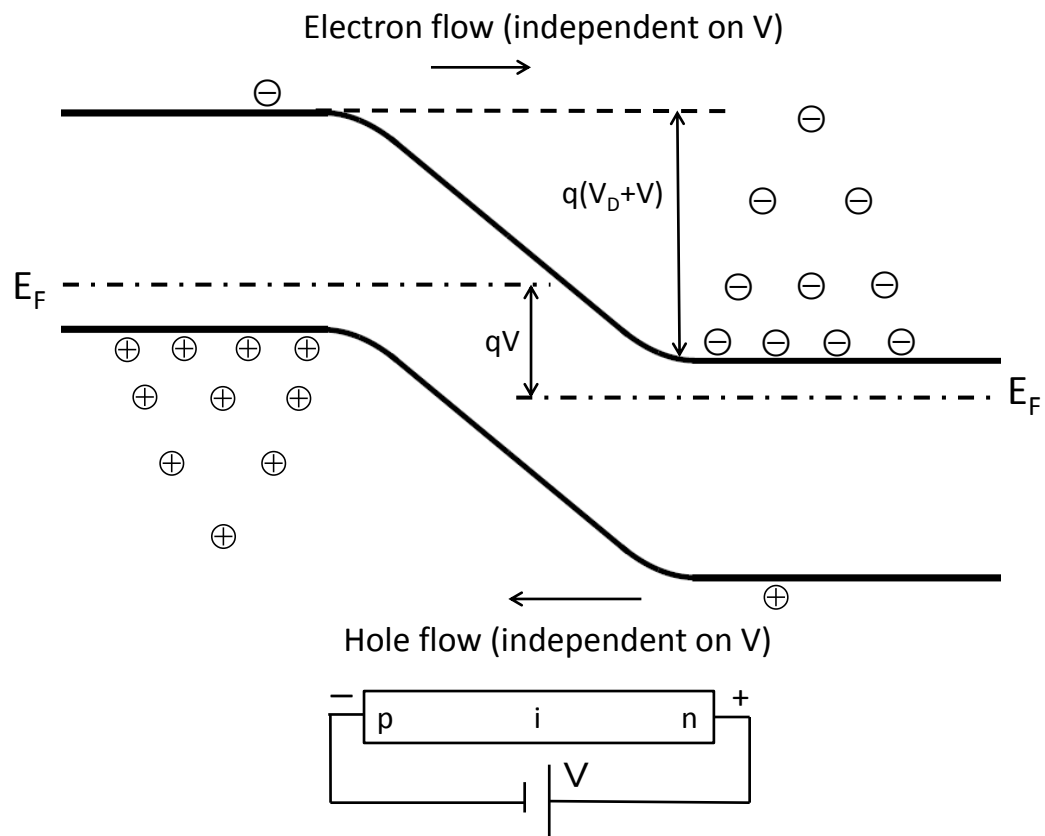


Figure 2.4: The electron flow and the hole flow.

$$J_e = -qK_1 e^{-qV_D/kT} (e^{-qV/kT} - 1) \quad (2.18)$$

$$= J_{e0} (e^{-qV/kT} - 1) \quad (2.19)$$

$$J_{e0} \equiv -qK_1 e^{-qV_D/kT} \quad (2.20)$$

In a similar way, the hole current density  $J_h$  can be represented as

$$J_h = J_{h0} (e^{-qV/kT} - 1) \quad (2.21)$$

$$J_{h0} \equiv -qK'_1 e^{-qV_D/kT} \quad (2.22)$$

The current density of the PIN diode is the sum of  $J_e$  and  $J_h$ .

$$J = J_e + J_h = (J_{e0} + J_{h0}) (e^{qV/kT} - 1) = J_0 (e^{qV/kT} - 1) \quad (2.23)$$

$$J_0 \equiv J_{e0} + J_{h0} \quad (2.24)$$

Fig.2.5 shows the plot. It is called the diffusion current.

The diffusion voltage,  $V_D$  depends on the temperature and the impurity concentration according to (2.13). The  $J_{e0}$  dependence on temperature and impurity concentration is derived below for later analysis. Substituting (2.2), (2.5), (2.7), and (2.13) into (2.20),

$$J_{e0} = -qK_1 e^{-\ln \frac{N_A N_D}{n_i^2}} \quad (2.25)$$

$$= -qK_1 \frac{n_i^2}{N_A N_D} \quad (2.26)$$

$$= -qK_1 \frac{N_C N_V}{N_A N_D} e^{-E_g/kT} \quad (2.27)$$

$$= \frac{I_0}{N_A N_D} T^3 e^{-E_g/kT} \quad (2.28)$$

Here,  $E_g = E_C - E_V$  and  $I_0 = -qK_1 \cdot 4 \left( \frac{4\pi^2 k^2 m_e^* m_h^*}{h^4} \right)^{2/3}$ . The calculation for hole current is similar to the electron current.

In the reality, there are other current components except diffusion current. The empirical expression of the current is as follows.

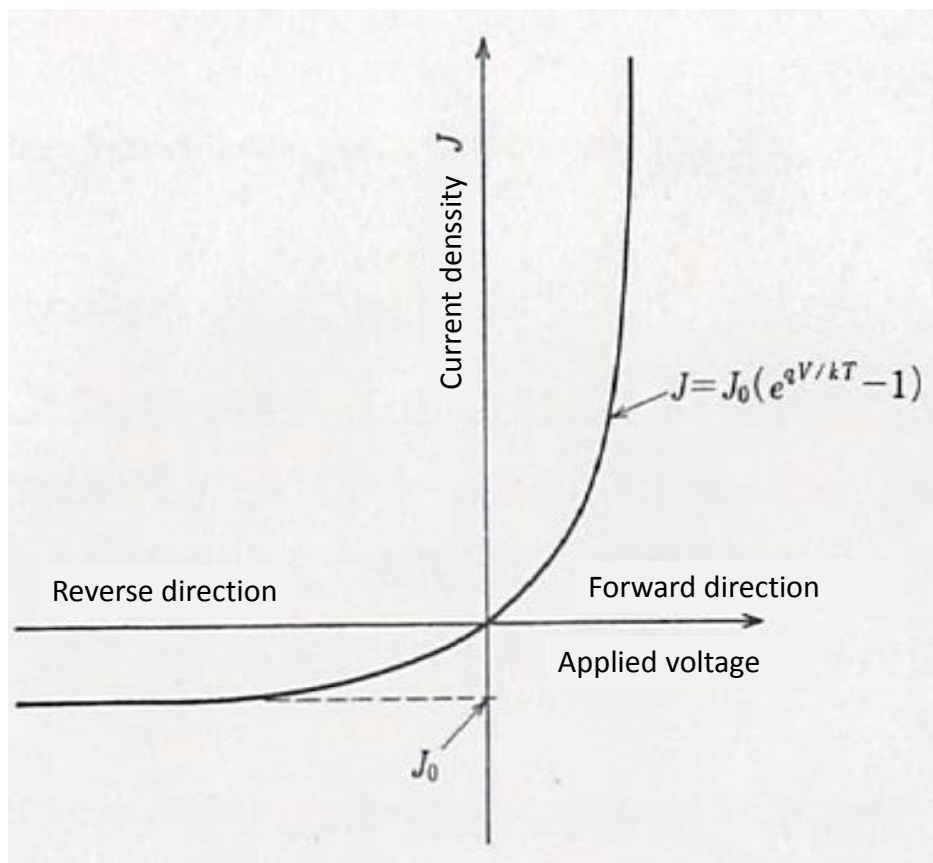


Figure 2.5: Current-voltage plot of (2.23). [4]

$$J = \frac{I_0}{N_A N_D} T^3 e^{-E_g/kT} (e^{\alpha qV/kT} - 1) \quad (2.29)$$

Here,  $\alpha$  is a constant usually between 0.5 and 1. In the low bias voltage region, the causes of  $\alpha$  are current components other than diffusion current. At a high bias voltage, the cause of  $\alpha$  is the series resistance component.

According to the discussion above, the leak current value, the fluctuation of the leak current, and the breakdown voltage can be measured by current-voltage measurement. The current-voltage properties also provide information about the impurity concentration, in particular the product of donor and acceptor concentration,  $N_A N_D$  according to (2.28).

### 2.2.3 Capacitance-voltage property

In this section, the dependence of the diode capacitance on the applied reverse bias voltage is discussed. When the silicon sensor has a depletion layer, there is charged volume. The p-type layer has a negatively charged volume and the n-type layer has a positively charged volume. This gives a capacitor-like property to the silicon sensor.

Here, it is assumed that the doping concentration changes as a step function, as shown in the bottom picture of Fig.2.6.

Then, the energy band chart is like the centre picture of Fig.2.6. The x-coordinate is defined from p-type toward n-type. The origin is set on the border between the depletion layer and the p-type layer. The P-I junction plane is  $x = x_1$ , I-N junction plane is  $x = x_2$ , and the border between the depletion layer and the n-type layer is  $x = x_3$ . Here, a constant  $d_I = x_2 - x_1$  is defined as a thickness of intrinsic layer.

The potential follows Poisson's equation:

$$\frac{d^2 v(x)}{dx^2} = -\frac{\rho}{\epsilon_s \epsilon_0} \quad (2.30)$$

$$\rho = \begin{cases} -qN_A & (0 \leq x < x_1) \\ 0 & (x_1 \leq x < x_2) \\ qN_D & (x_2 \leq x \leq x_3) \end{cases}$$

The boundary conditions are

$$\begin{cases} v(0) = 0, \frac{\partial v(0)}{\partial x} = 0 & (x = 0) \\ v(x) \text{ and } \frac{\partial v(x)}{\partial x} \text{ is continuous} & (x = x_1, x_2) \\ v(x_3) = V + V_D, \frac{\partial v(x_3)}{\partial x} = 0 & (x = x_3) \end{cases}$$

From Poisson's equation and the boundary conditions,

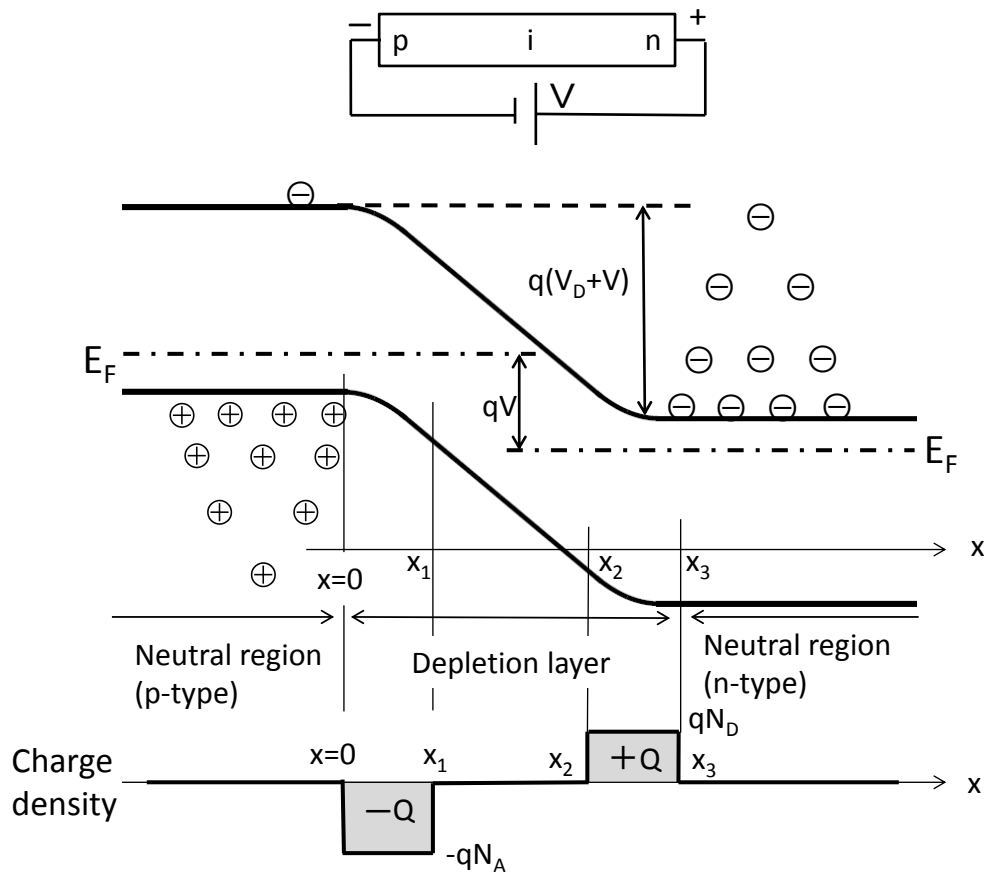


Figure 2.6: Energy band chart and the charge density distribution of PIN diode.

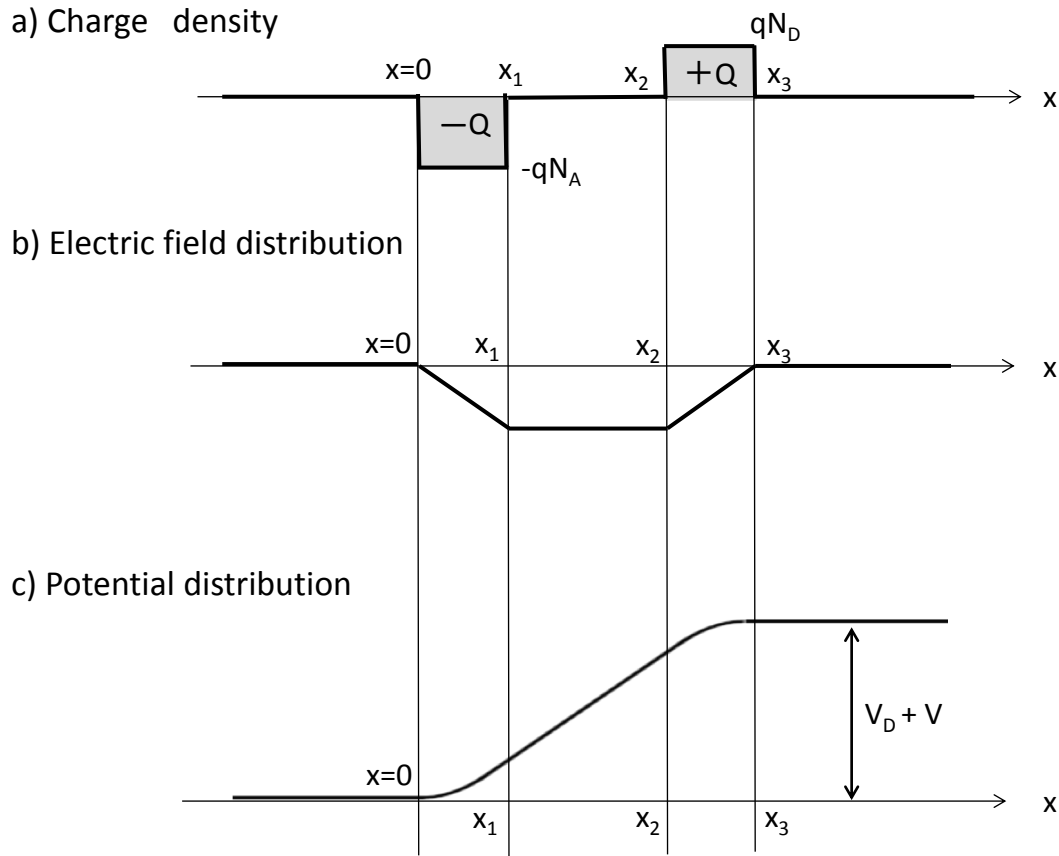


Figure 2.7: a) Charge density distribution. b) Electric field distribution. c) Potential distribution.

$$qN_A x_1 = qN_D (x_3 - x_2) \quad (2.31)$$

It means that the total number of positive charges and negative charges are equal. Moreover, the depletion layer width is inversely proportional to the impurity concentration. The electric field distribution is as in Fig.2.7 b).

In addition, following equation can be derived.

$$V + V_D = -\frac{qN_A}{2\epsilon_s\epsilon_0}x_1^2 + \frac{qN_A}{\epsilon_s\epsilon_0}x_1d_I + \frac{qN_D}{2\epsilon_s\epsilon_0}(x_3 - x_2)^2 \quad (2.32)$$

$$= \frac{qN_A}{2\epsilon_s\epsilon_0N_D}(N_A + N_D) \left( x_1 + \frac{N_D}{N_A + N_D}d_I \right)^2 - \frac{qN_AN_D}{2\epsilon_s\epsilon_0(N_A + N_D)}d_I^2 \quad (2.33)$$

The potential is shown in Fig.2.7 c).

The relation between the reverse bias voltage and total depletion width is

$$x_1 = \sqrt{\left( V + V_D + \frac{qN_AN_D}{2\epsilon_s\epsilon_0(N_A + N_D)}d_I^2 \right) \frac{2\epsilon_s\epsilon_0N_D}{qN_A(N_A + N_D)} - \frac{N_D}{N_D + N_A}d_I} \quad (2.34)$$

From this equation,

$$Q(V) = qN_Ax_1 \quad (2.35)$$

$$= \sqrt{\left( V + V_D + \frac{qN_AN_D}{2\epsilon_s\epsilon_0(N_A + N_D)}d_I^2 \right) \frac{2q\epsilon_s\epsilon_0N_AN_D}{N_A + N_D} - \frac{qN_AN_Dd_I}{N_A + N_D}} \quad (2.36)$$

Therefore,

$$C = \frac{dQ}{dV} = \sqrt{\frac{1}{V + V_D + \frac{qN_AN_D}{2\epsilon_s\epsilon_0(N_A + N_D)}d_I^2}} \sqrt{\frac{q\epsilon_s\epsilon_0N_AN_D}{2(N_A + N_D)}} \quad (2.37)$$

This  $C$  is the depletion-layer capacitance. It also can be represented as

$$\frac{1}{C^2} = \frac{2(N_A + N_D)}{q\epsilon_s\epsilon_0N_AN_D} \left( V + V_D + \frac{qN_AN_D}{2\epsilon_s\epsilon_0(N_A + N_D)}d_I^2 \right) \quad (2.38)$$

$$\equiv \frac{2(N_A + N_D)}{q\epsilon_s\epsilon_0N_AN_D} (V + V_0) \quad (2.39)$$

Here,  $V_0 = V_D + \frac{qN_AN_D}{2\epsilon_s\epsilon_0(N_A + N_D)}d_I^2$ . The expected curve of  $1/C^2$  against the reverse bias voltage is shown in Fig.2.8.

As in (2.39), the capacitance depends on the diffusion voltage and impurity concentration of both p-type layer and n-type layer. Moreover, the capacitance can be written as

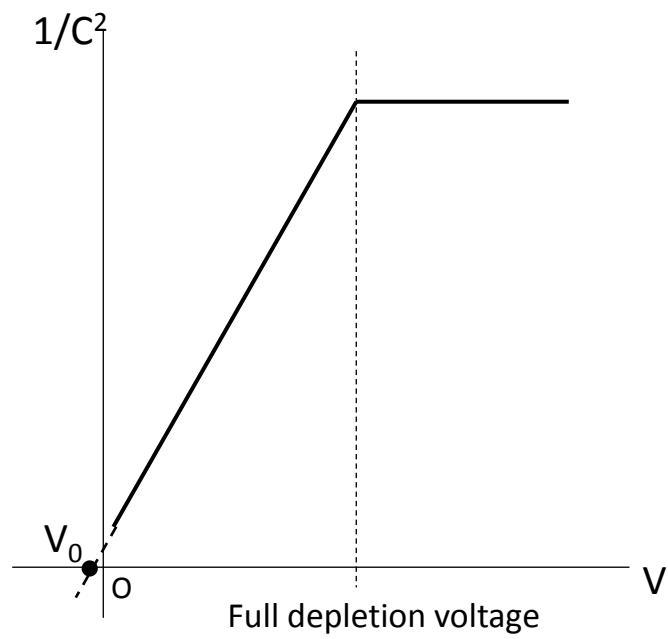


Figure 2.8: Theoretically expected curve of  $1/C^2$  against the reverse bias voltage  $V$ .

$$C = \frac{A\epsilon_s\epsilon_0}{d} \quad (2.40)$$

Here,  $A$  is the area of the sensor,  $\epsilon_0$  is the permittivity of the vacuum,  $\epsilon_s$  is the relative permittivity of silicon, and  $d$  is the thickness of the depletion layer. The thickness of the depletion layer can therefore also be measured.

The capacitance-voltage property measurement is used to measure the values  $V_0$  and  $\frac{N_A+N_D}{N_A N_D}$ , which depend on the impurity concentration and depletion thickness.

### 2.2.4 Signal collection

When a charged particle passes through the silicon sensor, it deposits energy, creating electron-hole pairs. The number of e-h pairs depends on only the deposited energy.

MIP deposit energy in silicon is  $1.664 \text{ MeV}\cdot\text{cm}^2/\text{g}$  [5]. The silicon thickness in our silicon sensor is  $320 \mu\text{m}$ . The density of silicon is  $2.3290 \text{ g}\cdot\text{cm}^{-3}$ . Therefore, energy deposit in silicon is  $0.124 \text{ MeV}$ . The e-h pair creation energy is  $3.64 \text{ eV}$ . Therefore, the number of e-h pairs will be  $3.41 \times 10^4$ . The total charge is  $5.45 \times 10^{-15} \text{ C}$ .

To get full depletion and to prevent recombination of the created e-h pairs, an electric field is applied. Then, e-h pairs are separated by electric field and collected in the electrode.

As discussed later in Sec.2.3, signal collection efficiency will decrease after irradiation. The signal collection efficiency can be measured using a radioactive source or cosmic rays.

## 2.3 Expected effects by radiation exposure

There are three types of radiation damage effects on silicon detectors: the total ionizing effect, the displacement damage dose effect, and the single event effect [6].

The total ionizing effect is caused by gamma-rays. When charged particles pass through the silicon sensor, e-h pairs are created as discussed in Sec.2.2.4. The mobility of electrons is very large, so they quickly arrive at the electrode. However, the mobility of holes is 5-6 orders of magnitude smaller than that of electrons. The holes are swept slowly. During sweeping, a hole may become trapped by a defect due to absent of oxygen around the interface between Si and  $\text{SiO}_2$  in the case of MOS (Metal-Oxide-Semiconductor) capacitor. Thus positive fixed charge is made. Fixed charges shift the capacitance-voltage curve to lower bias voltage, as if the positive fixed charge gives a positive bias voltage. In addition, interface state is also made in the band gap at the interface between Si and  $\text{SiO}_2$  by the total ionizing effect. The interface state is produced when a Si atom has a dangling bond which is not bonded by covalent bond with O atom. Interface states charge positively for voltages smaller than the mid gap voltage and negatively for voltages higher than mid gap voltage. The mid gap voltage is the voltage at which all the interface states are neutral. The interface states make

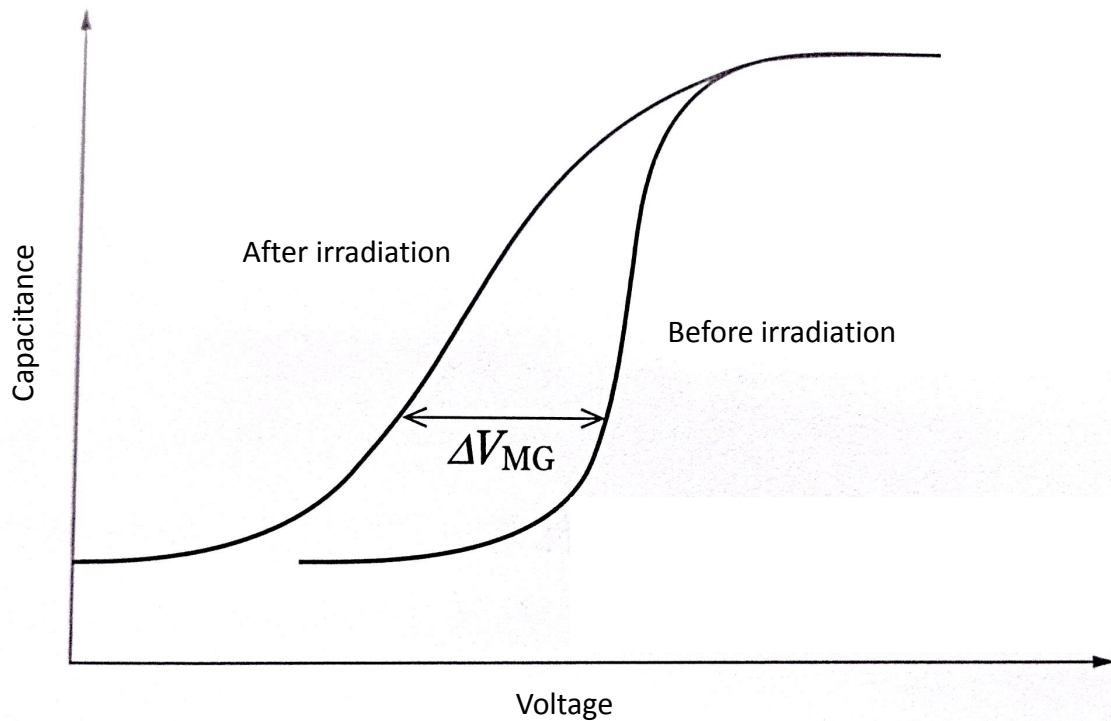


Figure 2.9: Expected capacitance-voltage property change by irradiation.[6]

the capacitance-voltage curve gradual. The number of fixed charges and interface states increases as the radiation dose increases. The effect of total ionizing effect is expected to be like Fig.2.9 for MOS capacitor.

There is MOS (Metal-Oxide-Semiconductor) structure in the p-type side of our silicon sensor. From the surface, metal as an electrode, silicon oxide as a insulator, and semiconductor are placed. The MOS capacitor-like property can be seen at a low reverse bias voltage.

These total ionizing effects are evaluated with the absorbed dose, defined by

$$D_e = \frac{dE}{dm} [\text{J/kg}] \quad (2.41)$$

Here,  $E$  is absorbed radiation energy and  $m$  is mass. The unit is Gy [1 Gy = 1 J/kg].

Secondly, displacement damage dose effects are caused by high energy particles such as neutron, electron, heavy ion, and gamma-ray. Charged particles lose most of their energy

by inelastic scattering, ionization and bremsstrahlung. The probability of elastic scattering is much smaller than inelastic scattering. For the most part in elastic scattering, induced particles give very little energy to the nucleus. In the rare case when large momentum is transferred to a nucleus, a crystal atom is displaced. The displaced atom is called a Primary Knocked-on Atom (PKA). It creates a point defect. The original position of the PKA also becomes a point defect (vacancy defect). The number of these defects increases as the radiation dose increases. Some defects couple with other defects or impurities. Others couple with void and pair annihilation occurs. Finally, many kinds of complex defects are made. These defects create energy states called creation-recombination centres in the band gap. The lifetime and mobility of electrons and holes are decreased by creation-recombination centres, causing an increase of leakage current and decreasing signal charge.

Some of the defects from displacement catch majority carriers. If the density of such defects increases to the order of the original carrier concentration, the state becomes carrier exhausted. Generally, carrier exhaustion has the relation

$$p_\phi = p_0 - R_c \phi \quad (2.42)$$

or

$$p_\phi = p_0 e^{-R_c \frac{\phi}{p_0}} \quad (2.43)$$

Here,  $\phi$  is the particle fluence and  $p_0$  is the carrier concentration before irradiation.  $R_c$  is called the carrier exhaustion coefficient, representing the magnitude of the carrier concentration decreasing effect.

The absorbed dose is not appropriate for evaluating the displacement damage dose effect. It is because absorbed dose is based on energy given via ionization, but cause of the displacement damage dose effect is displacement of an atom consisting the crystal. The displacement damage dose  $D_d$  is suggested for evaluating it.

$$D_d = \phi \cdot NIEL [\text{MeV/g}] \quad (2.44)$$

The NIEL is the Non Ionizing Energy Loss, which depends on the energy of the incident particle. NIEL is given by the deposited radiation energy divided by the density of the irradiated substance. NIEL is defined as follows.

$$NIEL(E_{in}) = \frac{1}{M} \int_{E_d}^{E_{p(max)}} \frac{d\sigma_p}{dE_p} E_p L \cdot dE_p [\text{eV} \cdot \text{cm}^2/\text{g}] \quad (2.45)$$

Here,  $E_{in}$  is the energy of the incident particle,  $M$  is the mass of the irradiated substance, and  $\frac{d\sigma_p}{dE_p}$  is the differential displacement cross section.  $E_p$  is the displacement energy given to the target atom by a collision.  $L$  is a value without dimension called the Lindhard partition factor.  $E_d$  is the threshold energy of displacement and  $E_{p(max)}$  is the maximum displacement

energy. There is more detailed discussion about NIEL in App.A.

Thirdly, single event upsets are caused by alpha-rays, heavy ions and neutrons. Heavy ions have high stopping power. When it enters the p-n junction in the IC (Integrated Circuit) for electronics, it creates e-h pairs with high density. It causes a transient current. If it occurs in silicon sensor, it is no problem in our case because it is normal calorimeter operation. However, if it occurs in readout electronics, it is a problem. Generally, the time scale of the transient current is on the order of 10 ps - 1 ns. It can change the operating state of the IC. Thus it causes many kinds of single event effects such as malfunction. In the case of neutron, nuclear reactions occur with very small probability. Thus it creates heavy ions as fission products. The heavy ions causes single event upset as mentioned above.

There are three types of radiation damage as discussed above. However, total ionizing dose effect does not affect to the PIN diode operation because it creates defects mainly between semiconductor and semiconductor oxide. The single event effect also does not provide any problem because this effect is normal calorimeter operation. The most important effect is the displacement damage dose effect.

The neutron irradiation damage for silicon semiconductor detectors will be tested to measure the displacement damage dose effect. The expected effects from radiation damage are increased leakage current, effective impurity decreasing by carrier exhaustion, and deterioration of signal collection efficiency.

## 2.4 The requirement for silicon sensor for the ILD ECAL

The requirement for the silicon sensor is discussed in this section from the point of view of irradiation effect.

First, the leakage current should be low and stable at the operation reverse bias voltage. It is required for low and stable noise. Secondly, sufficiently higher breakdown voltage than the operation reverse bias voltage. Breakdown is that current increases steeply from a certain reverse bias voltage. If the breakdown voltage is near the operation reverse bias voltage, it leads to unstable high leakage current. Thirdly, full depletion is achieved at the operation reverse bias voltage. It is required to get the maximum sensitive volume. Fourthly, enough signal collection efficiency. It directly affects to the energy measurement. It also affects to the number of noisy pixels because the MIP signal decreases and the signal threshold is set to 0.5 MIP. More detailed discussion about the requirement for signal collection efficiency will be given in Sec.6.3. The last, PIN diode property should be kept. The impurity concentration should be same order before and after irradiation.

Summarizing above, the silicon sensor properties is evaluated by leakage current  $I_D$ , capacitance  $C$ , and charge collection efficiency  $\epsilon$ . Detailed measurement method will be discussed in later chapters.

# Chapter 3

## Current-voltage measurement

The current-voltage measurement is described in this section. The leakage current and the breakdown voltage can be directly measured. Combined with temperature dependence, impurity concentration related value was measured. The leakage current is expected to increase after irradiation. The impurity concentration is expected to decrease or type inversion may occur after irradiation.

### 3.1 Setup

The setup for current-voltage measurement is shown in Fig.3.1. A photograph of the measurement box is shown in Fig.3.2. It was used to fix the position of the silicon sensor. The upper picture of Fig.3.2 is the cover of the measurement box. It has  $16 \times 16$  thin pins which are connected to each pixel in the silicon sensor. All pins are connected to a common electrode at the back of the black board. The bottom picture of Fig.3.2 shows the case for the silicon sensor. The bottom of the case has a second common electrode which is in contact with the other side of the sensor. A high reverse bias voltage is applied between the upper side and bottom side of the measurement box. The measurement box was designed for the main chip with 256 pixels. To measure the smaller baby chips, a sheet of plastic was used to insulate unused pins. The measurement box was placed in a black box, since the diodes are sensitive to light. A Keithley2410 high-voltage source meter [7] was used to apply a high reverse bias voltage and measure the resulting current. The detailed specification of the Keithley2410 high-voltage source meter is summarized in App.B. The source meter was controlled via a GPIB interface. The temperature was measured using a thermocouple attached to the ground electrode just under the silicon sensor. The measurement was executed in room temperature and the temperature was not controlled.

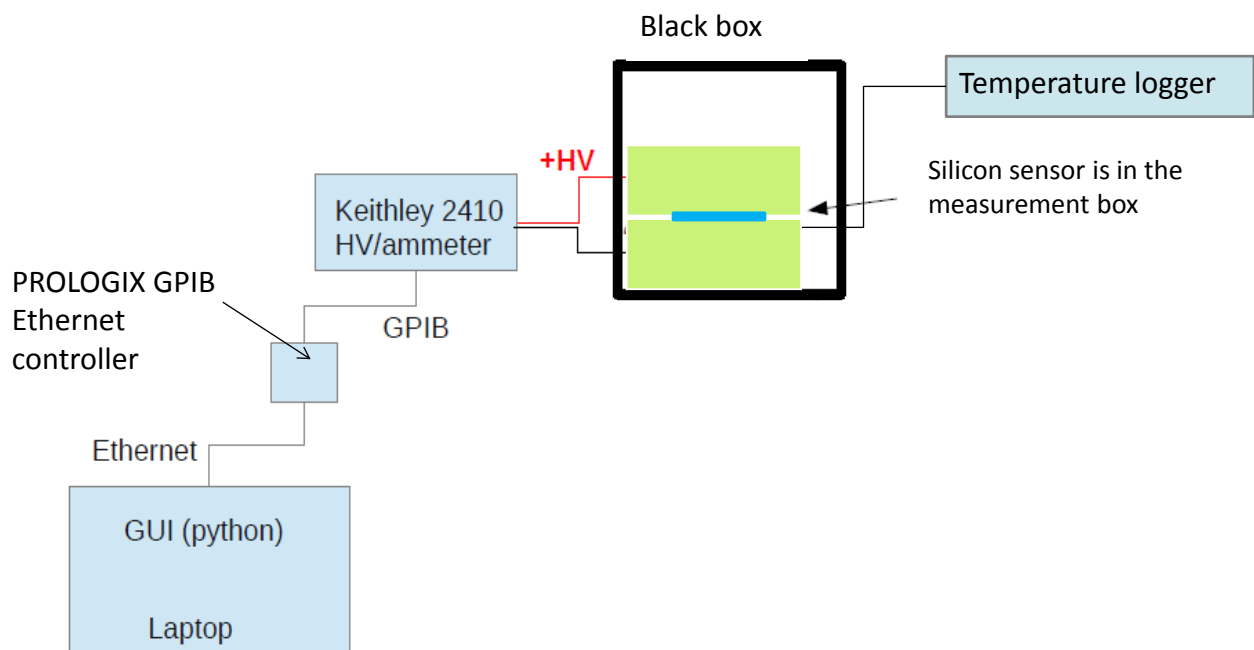


Figure 3.1: Setup for current-voltage measurement

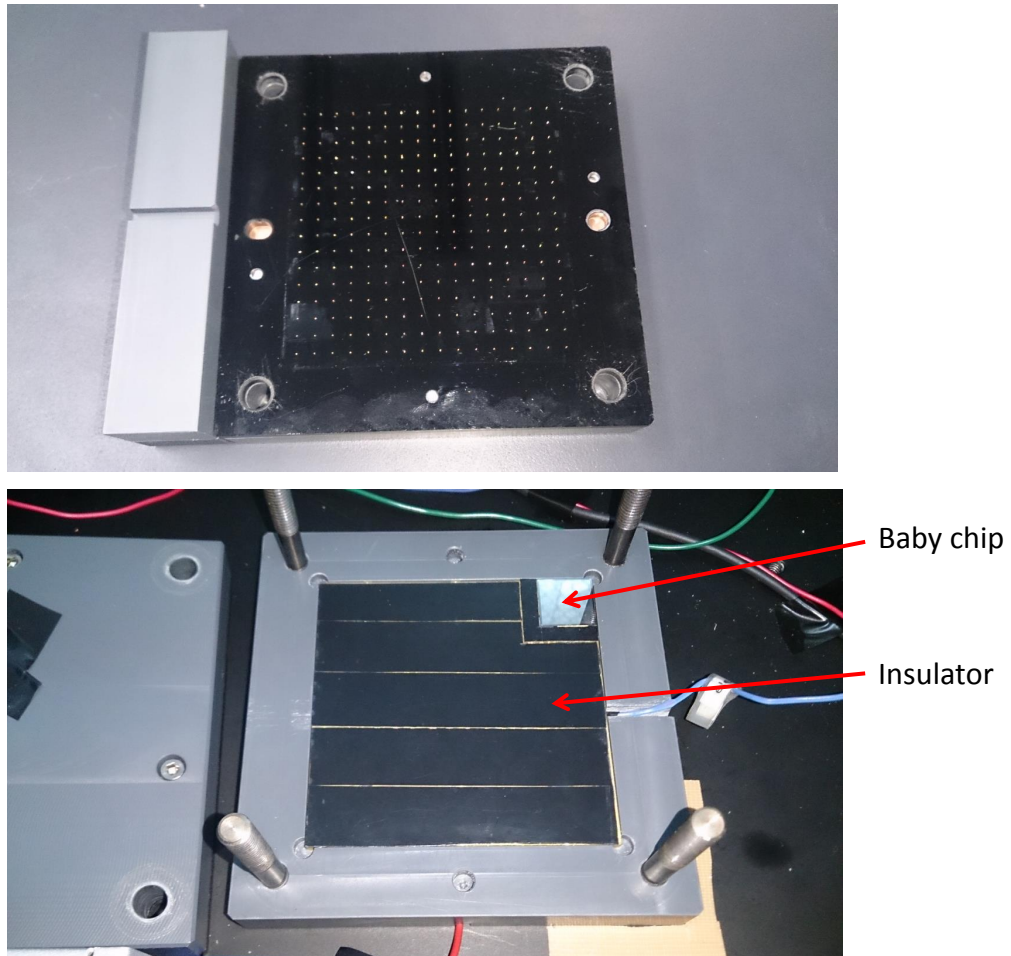


Figure 3.2: A photograph of the measurement box. Upper picture is the cover and bottom picture is the case with baby chip and insulator.

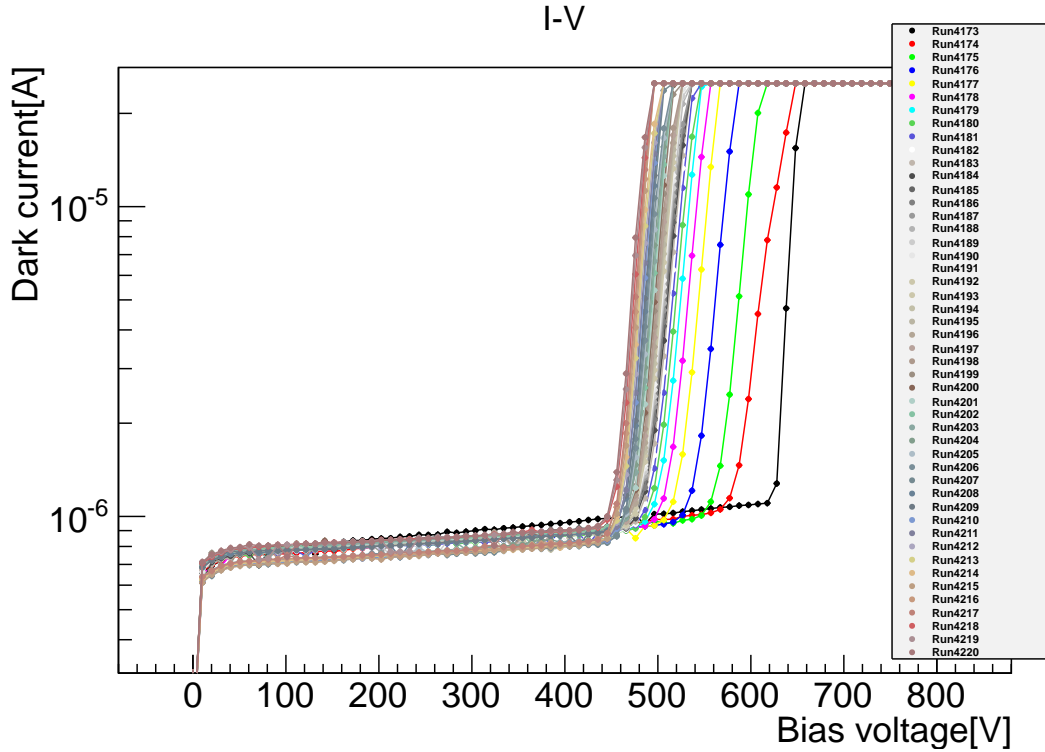


Figure 3.3: Current-voltage plot for main chip. The temperature changed from 23.9 °C at the first scan to 24.4 °C at the last scan.

## 3.2 Leakage current

Figs.3.3-3.6 show the results of the current-voltage measurement. To get these plots, the reverse bias voltage was increased in step of 10 V. At every step, the current was read 1 s after the reverse bias voltage change, and then increased to the next reverse bias voltage value. For main chip, the voltage is fixed if the measured current reached 25  $\mu\text{A}$ . For baby chips, the scan was terminated if either the measured current exceeded 100 nA or the reverse bias voltage reached 800 V. At the completion of a scan, the sensor was left unpolarized for 60 s before the scan was repeated. Voltage scans were repeated 39 times in succession.

The current almost saturates around 50 V. At the operation reverse bias voltage, full depletion and stable leakage current are required for reliable operation as discussed in Sec.2.4. Stable leakage current means that the reverse bias voltage should be well below the breakdown voltage. For main chip, a steep increase of current is seen from around 450-600 V. This phenomenon is called breakdown. It was only seen in some of the scans. This breakdown behaviour is not stable because the leakage current changes largely by small reverse bias voltage fluctuation. For baby chip 1-1, the breakdown voltage is about 750 V. For the other baby chips, 1-2 and 2-1, no breakdown behaviour was observed at voltages up to 800 V. Experimentally, the operation reverse bias voltage is set to about 120 V. At 120 V, the mean

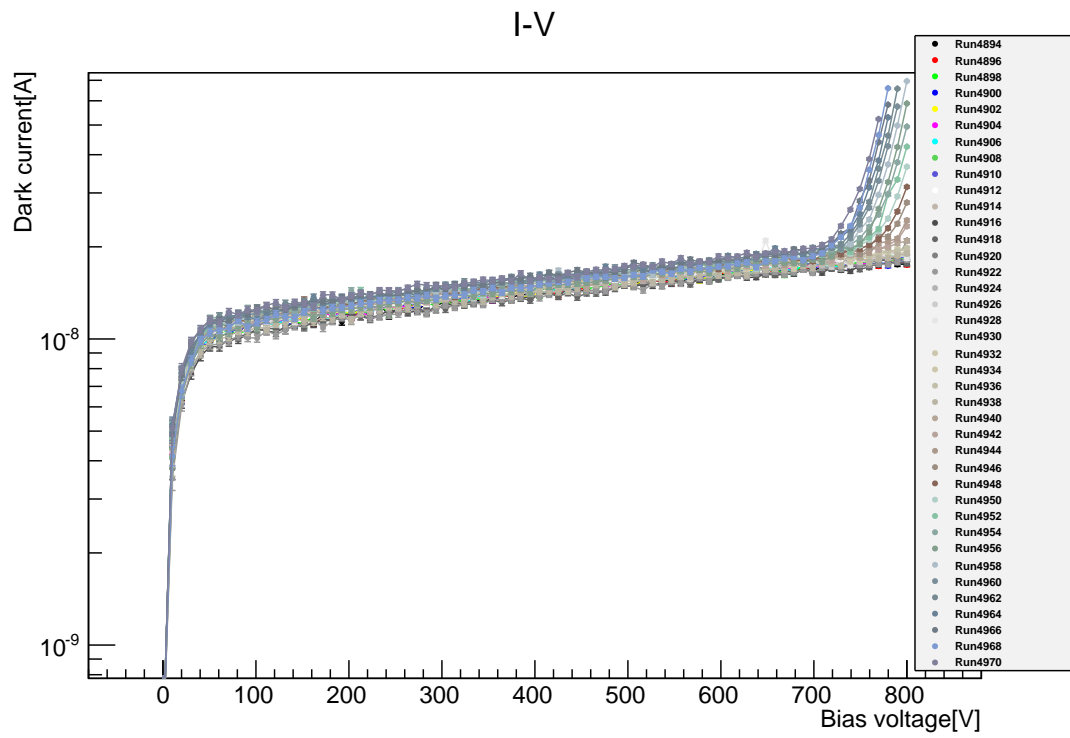


Figure 3.4: Current-voltage plot for baby chip 1-1. The temperature changed from 25.0 °C at the first scan to 25.8 °C at the last scan.

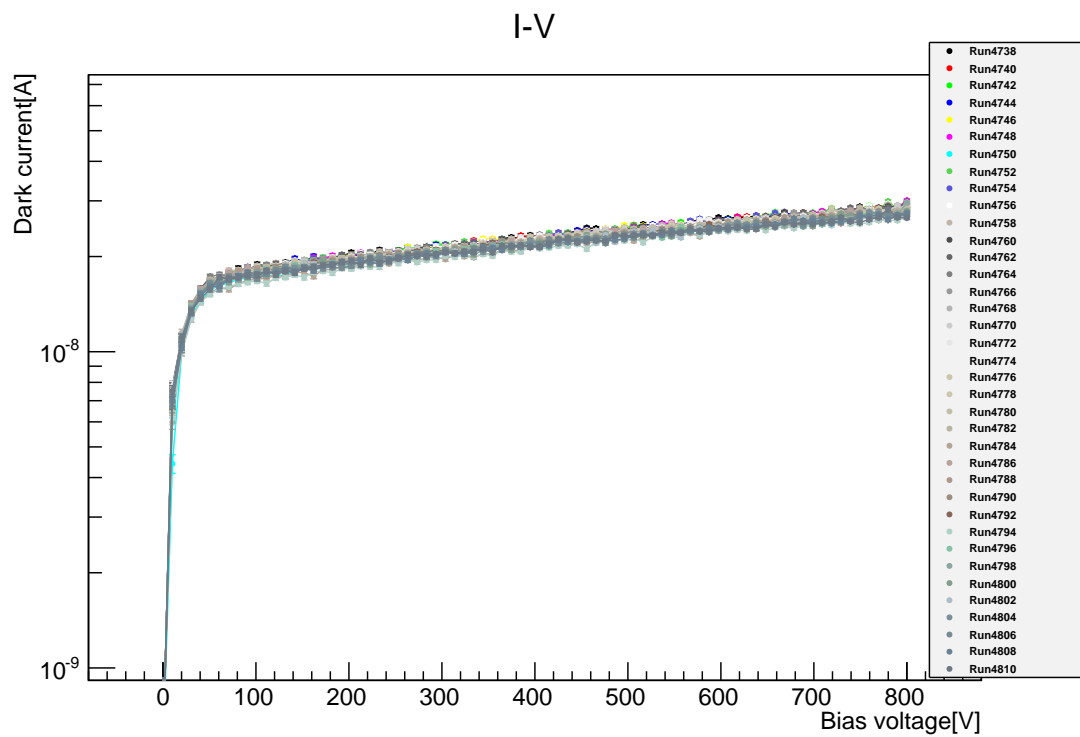


Figure 3.5: Current-voltage plot for baby chip 1-2. The temperature changed from 26.3 °C at the first scan to 25.4 °C at the last scan.

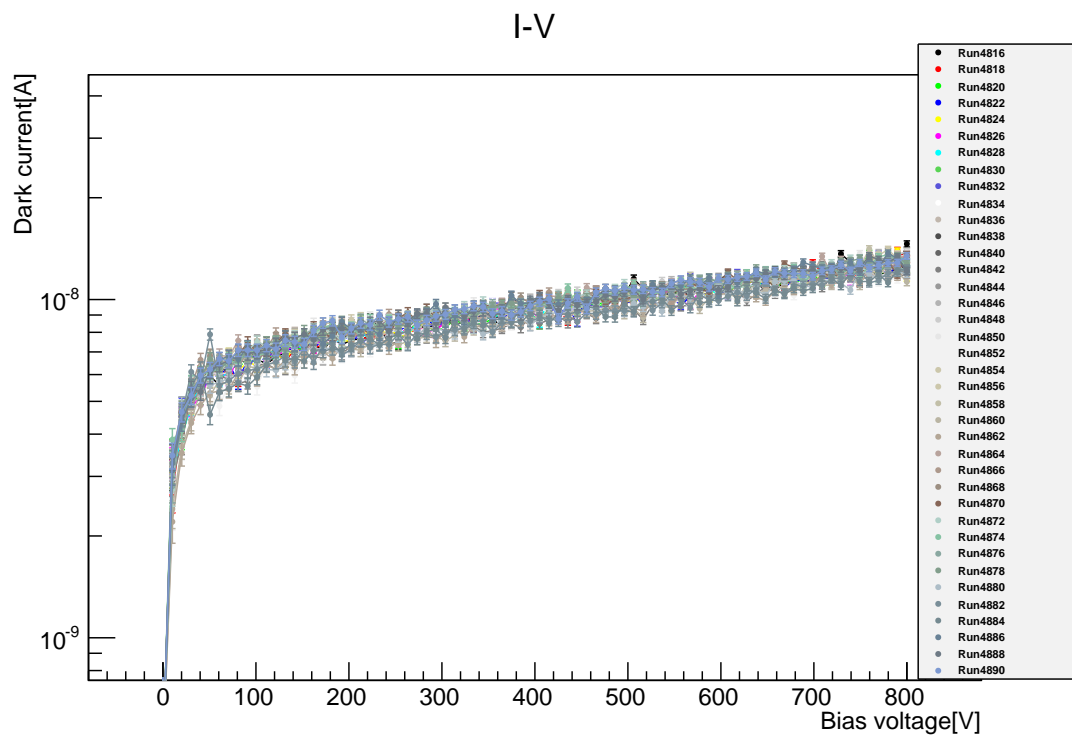


Figure 3.6: Current-voltage plot for baby chip 2-1. The temperature changed from 25.5 °C at the first scan to 25.8 °C at the last scan.

and RMS fluctuation of the leakage current measurement of main chip, each baby chip, 1-1, 1-2, and 2-1 were  $775 \pm 33$  nA,  $11.7 \pm 0.6$  nA,  $18.2 \pm 0.5$  nA, and  $7.1 \pm 0.4$  nA, respectively. These fluctuations correspond respectively to 4.3%, 4.8%, 2.5%, and 5.6%. If the rise time of the pre-amplifier is 30 ns[11], the leakage current gives additional  $9.09 \times 10^{-17}$  C per pixel to the signal for main chip, which has the largest leakage current of the four. It is 50 times lower than MIP signal,  $5.45 \times 10^{-15}$  C. Therefore, this result is tolerable for the ILD ECAL.

### 3.3 Temperature dependence

As shown in (2.29), the current depends on temperature as follows:

$$I = \frac{I_0}{N_A N_D} T^3 e^{-E_g/kT} (e^{\alpha qV/kT} - 1) \quad (3.1)$$

Here,  $\alpha$  is a constant usually between 0.5 and 1 [4].

The current was measured within a narrow voltage range between -0.25 V and 0.25 V many times for baby chip 1-2, allowing the behaviour to be investigated as a function of temperature. The result of one of these measurements is shown in Fig.3.7.

The statistical error of the current measurement was estimated based on the resolution of the Keithley2410 high-voltage source meter (see App.B) and the 2.5% of current fluctuation which is discussed in the sec.3.2. The systematic error of the current measurement was estimated based on the accuracy of the Keithley2410 high-voltage source meter (see App.B).

The data were fitted to a function of the form (3.1), by using the method of least squares, and used to estimate the factor. One value of  $\frac{I_0}{N_A N_D} T^3 e^{-E_g/kT}$  (equivalent to  $J_{e0}$  in (2.28)) can be gotten for each measurement. Fig.3.8 shows the dependence of this factor on temperature.

This temperature dependence was used to extract  $\frac{I_0}{N_A N_D}$ , assuming  $E_g = 1.1250$  eV [8]:

$$\frac{I_0}{N_A N_D} = 402.8 \pm 1.1(\text{stat.}) \pm 34(\text{syst.}) \text{ A} \cdot \text{K}^{-3} \quad (3.2)$$

Since this number depends on the impurity concentration, it will change with increasing irradiation. According to past studies [18]-[20], it is expected that  $10^{12}$  n/cm<sup>2</sup> neutron irradiation will result in an order of 10% decreasing of impurity concentration and a few  $10^{12}$  n/cm<sup>2</sup> neutron irradiation will cause type inversion.

The fits of the current-voltage curves also yield the factor  $\alpha$ . Fig.3.9 shows the dependence of  $\alpha$  on temperature. There is no significant dependence of  $\alpha$  on temperature. The average is  $0.9346 \pm 0.0003(\text{stat.}) \pm 0.013(\text{syst.})$ , within the expected range of 0.5-1 [4].

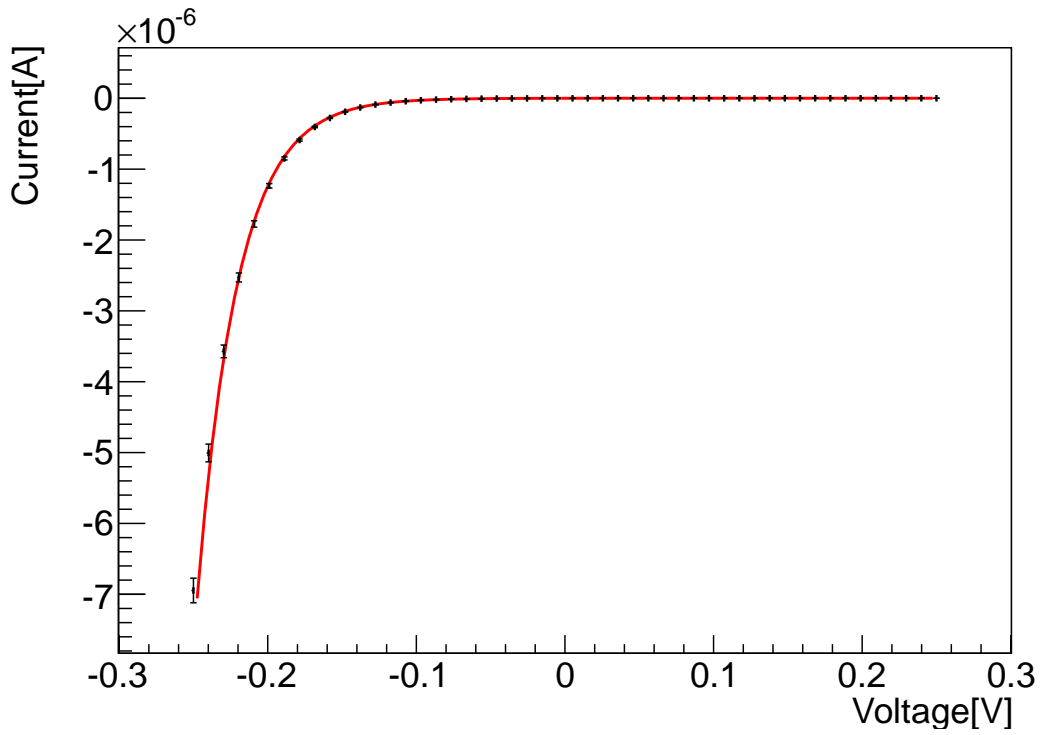
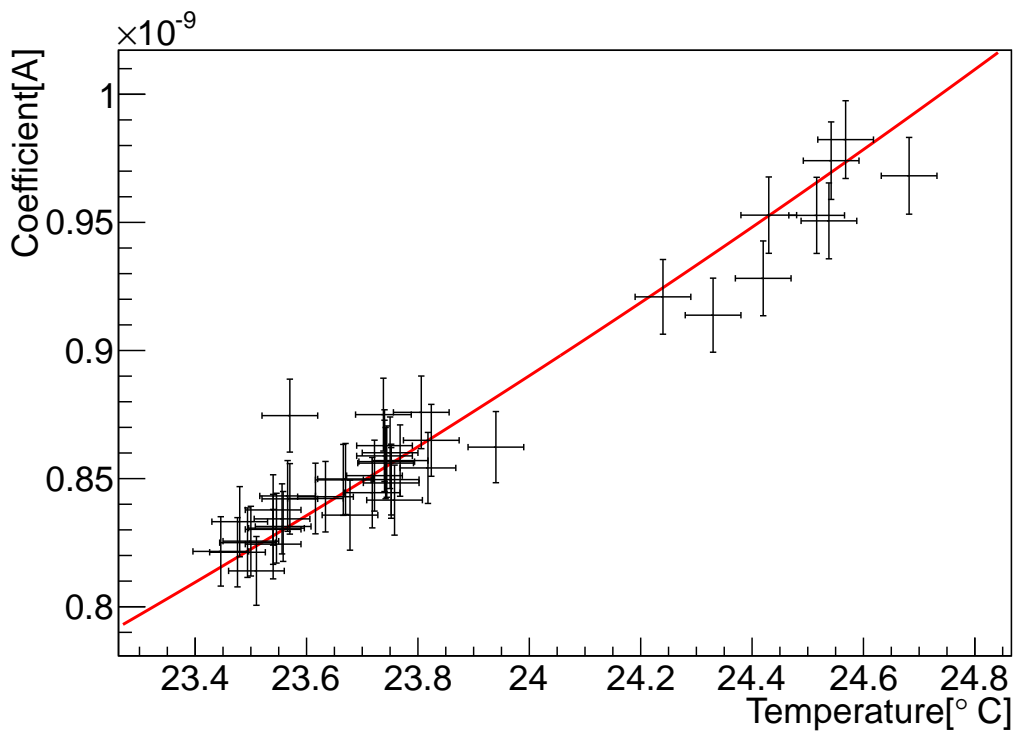


Figure 3.7: Current-voltage plot in low voltage.

Figure 3.8: The dependence of  $J_{e0}$  on the temperature.

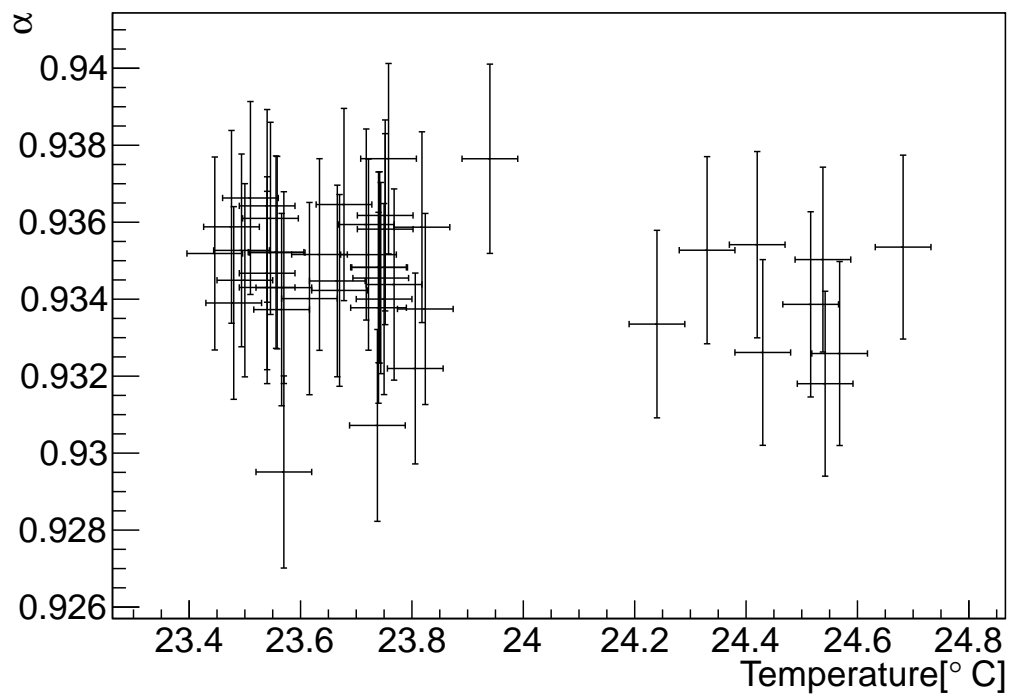


Figure 3.9: The dependence of  $\alpha$  on the temperature.

# Chapter 4

## Capacitance-voltage measurement

The capacitance-voltage measurement is described in this section. The full depletion voltage and the capacitance at the time are directly measured. The full depletion depth, the voltage offset  $V_0$  and the impurity concentration related value can be extracted from the measurement. The impurity concentration is expected to decrease or type inversion may occur after irradiation.

### 4.1 Setup

The setup for the capacitance-voltage measurement is described in Fig.4.1. An Agilent LCR meter was used for the capacitance measurement [9][10]. The detailed specification of the Agilent LCR meter is summarized in App.C. This instrument measures capacitance by using a four-terminal pair method. The four terminal pair have the name Hp, Hc, Lp, and Lc (H/L = high/low, p/c= potential/current). A Keithley2410 was used to apply a high reverse bias voltage.

Fig.4.2 shows the basis of the circuit inside the LCR meter. The "Device" is the silicon sensor in this measurement. The LCR meter applies an AC signal on the silicon sensor from the Hc terminal. The applied AC signal is measured through the Hp terminal. The resulting current through the sensor is measured by the Lc terminal. The capacitance is measured by comparing the input AC voltage and output current. The Lp terminal is set to ground using an auto-balance bridge and works to produce a current in the outer lead. This current is the same as the current in the silicon sensor and the inner lead. They cancel the magnetic field each other, thus suppressing its influence on the measurement.

Since the capacitance of the PIN diode depends on the reverse bias voltage, the signal AC voltage is set to a low voltage of 20 mV. An additional external circuit was used to isolate the LCR meter from the DC bias. This circuit also cuts the frequency component lower than 30 kHz, so a frequency of 100 kHz was used in the measurement. The capacitance

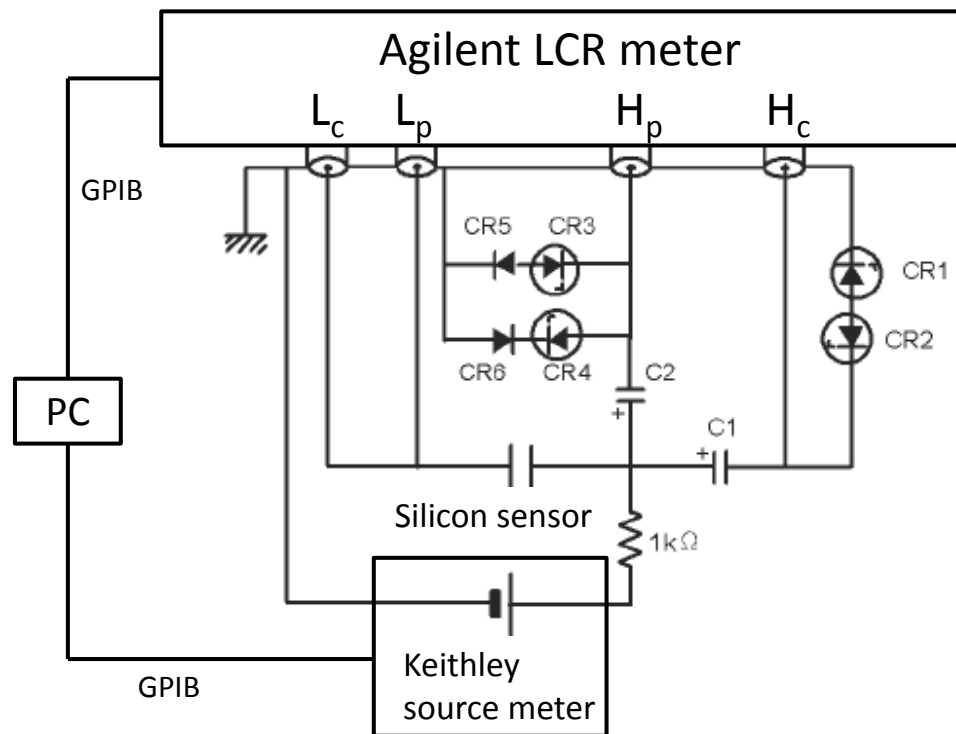


Figure 4.1: Setup for the capacitance-voltage measurement.  $C1$  and  $C2$  are  $1\ \mu\text{F}$  capacitors.  $CR1$  and  $CR2$  are zener diodes with 47 V of the zener voltage.  $CR3$  and  $CR4$  are zener diodes with 3.3 V of the zener voltage.  $CR5$  and  $CR6$  are rectifier diodes. [9]

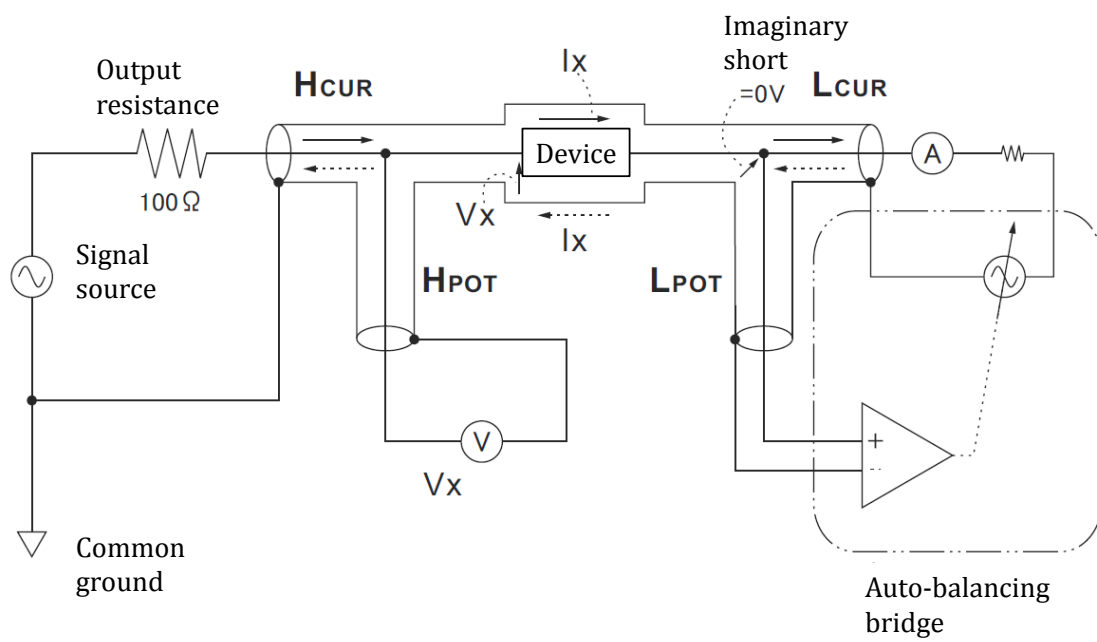


Figure 4.2: The circuit describing four-terminal pair method. [10]

measurements were made with an interval of 2 minutes because the capacitor in the external circuit required about 2 minutes to become stable.

## 4.2 Systematic error estimation study

According to [9], the error of the capacitance measurement is due to two components: the error from LCR meter itself, and that due to the measurement box [9]. The error components due to the LCR meter are the calibration accuracy, basic accuracy, sensor impedance effect, short offset, and open offset [10]. The calibration accuracy is  $0.03 + 1 \times 10^{-3} \times F_m \%$ . Here,  $F_m=100$  is frequency of the signal AC voltage, in units of kHz. The basic accuracy is  $0.1 \times \frac{30\text{mV}_{\text{rms}}}{V_s} \times K_t \%$ . Here,  $V_{\text{rms}}$  is an unit of voltage for signal level. The signal level  $V_s = 20 \text{mV}_{\text{rms}}$ .  $K_t = 1$  is a temperature coefficient. The sensor impedance effect is 0.05%. The short offset is  $0.6\text{m}\Omega(1+0.400/V_s)(1+\sqrt{1000/F_m})/Z_s \times 100\%$ . Here,  $Z_s$  is the impedance of the silicon sensor. The open offset is  $0.5\text{nS}(1+0.100/V_s)(1+\sqrt{100/F_m}) \times 100\%$ . The sum of these four components is the error due to the LCR meter.

The error components due to the measurement box is from the residual impedance. The external circuit and measurement box represent an additional impedance. To compensate its effect, the LCR meter performs open and short corrections. The open correction is done with the same setup except that the silicon sensor is replaced by an insulator, while the short correction is performed with the silicon sensor removed and the measurement box short-circuited. The LCR meter measures the residual impedance by these two types of corrections.

The error components due to the measurement box were estimated by measuring the reproducibility of the open state and the short state for the corrections. Fig.4.3 shows a plot of  $G = 1/R$  against  $-i\omega C$  measured with open state. The open reproducibility  $Y_0$  is defined as the distance of points from the origin (0,0). Fig.4.4 is a plot of  $R$  against  $-1/i\omega C$  with short state. The distance from the origin (0,0) is the short reproducibility,  $Z_0$ . Open and short measurements were performed one after another, with ten data points taken in each measurement. From these measurement, the open reproducibility  $Y_0 = 28 \text{ nS}$  and the short reproducibility  $Z_S = 4.3 \Omega$ . Their total contribution to the uncertainty is

$$Z_m = (P + \frac{Z_S}{Z_X} + Y_0 \cdot Z_X) \% \quad (4.1)$$

Here,  $Z_X$  is the impedance of the silicon sensor. In reality, there may be proportional component P to the impedance uncertainty. However, it can't be measured with our setup.

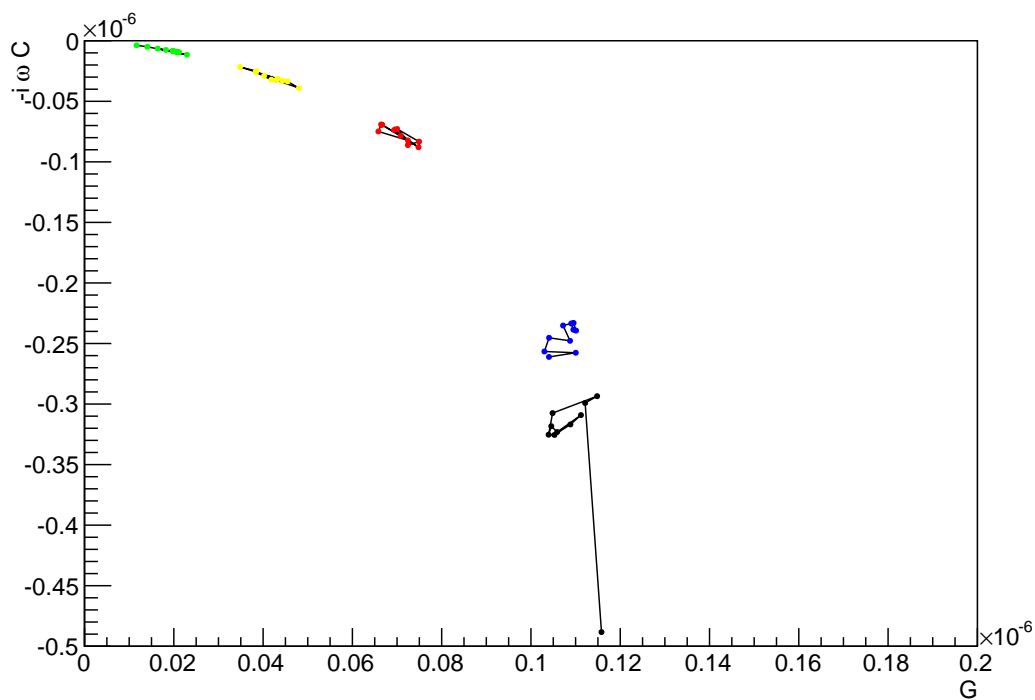


Figure 4.3: Reproducibility of open state. The same colour points were measured successively. The different colour points were measured after reconstruction of an open state.

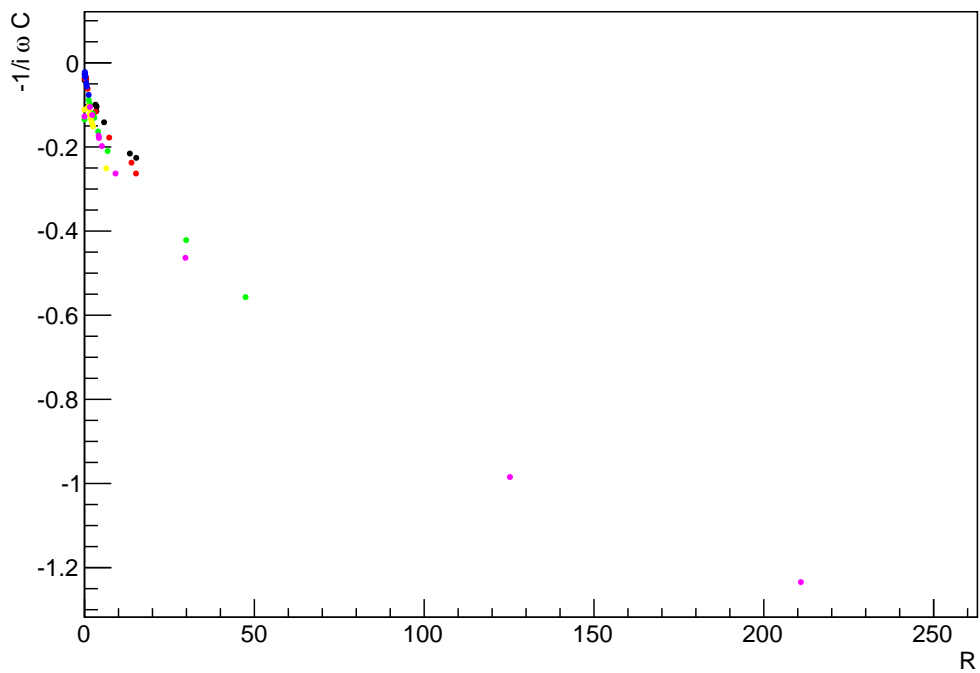


Figure 4.4: Reproducibility of short state. The same colour points were measured successively. The different colour points were measured after reconstruction of a short state.

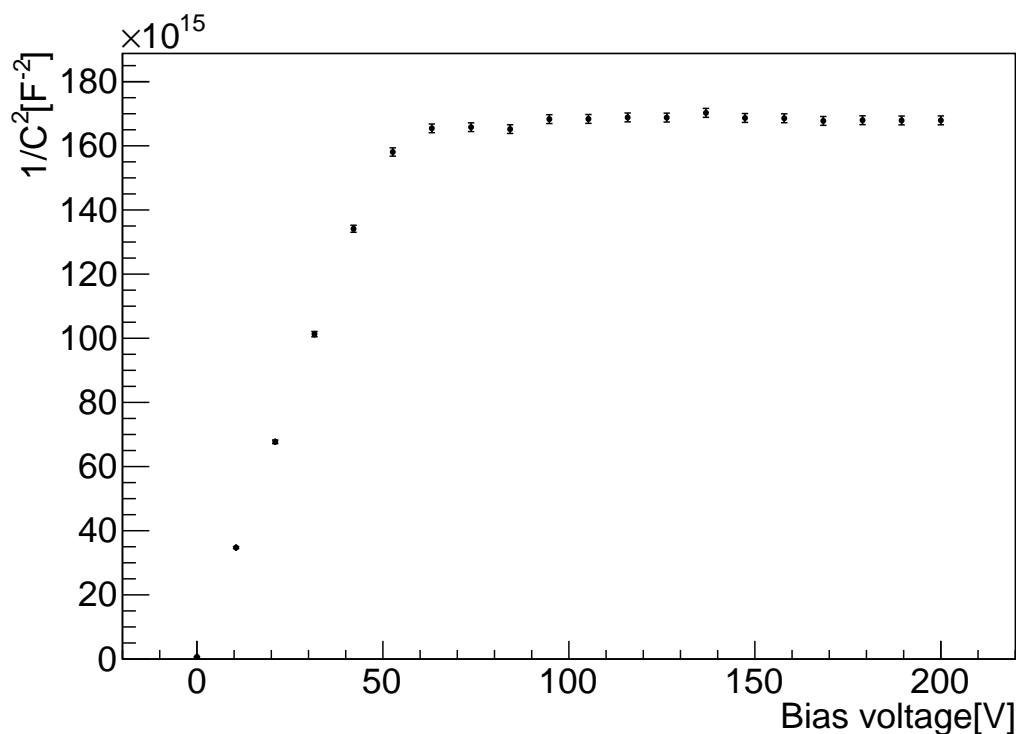


Figure 4.5: Capacitance-voltage plot for main chip.

### 4.3 Depletion width, diffusion voltage

The results of reverse bias voltage scans are shown in Figs.4.5-4.8, which show the dependence of the inverse squared capacitance  $1/C^2$  as a function of the applied reverse bias voltage  $V$ . As predicted by (2.39), a linear dependence of  $1/C^2$  on the reverse bias voltage is seen in the reverse bias voltage below around 50 V. The saturation at about 50 V is due to full depletion of the PIN diode. The statistical error of this measurement was estimated by considering the  $1/C^2$  fluctuations above 70 V. As shown in (2.40), the fully depleted capacitance allows the depletion layer depth to be estimated. The saturated capacitance is shown in the first row of Table 4.1, 4.2. The depletion thickness was calculated as in second row of Table 4.1, 4.2. Here, systematic uncertainty includes capacitance systematic error discussed in previous section and baby chip area error. The length of a side of the main chip is  $89.700 \pm 0.040$  mm. The length of a side of the baby chip is  $16.460 \pm 0.040$  mm. These result is not consistent with the thickness of the silicon sensor,  $320 \pm 15$   $\mu\text{m}$ . It may be temperature effect or the effect of proportional error component. More study is required.

As shown in (2.39), the value  $V_0 = V_D + \frac{qN_A N_D}{2\epsilon_s \epsilon_0 (N_A + N_D)} d_I^2$  gives rise to an offset in the linear region of Fig.4.6-4.8. The data were fitted to a straight line in the reverse bias voltage range from 8 V to 41 V.  $V_0$  is shown in the third row of the Table 4.1, 4.2. The result seems not consistent among the 3 baby chips, more study is required. In addition, the slope of the

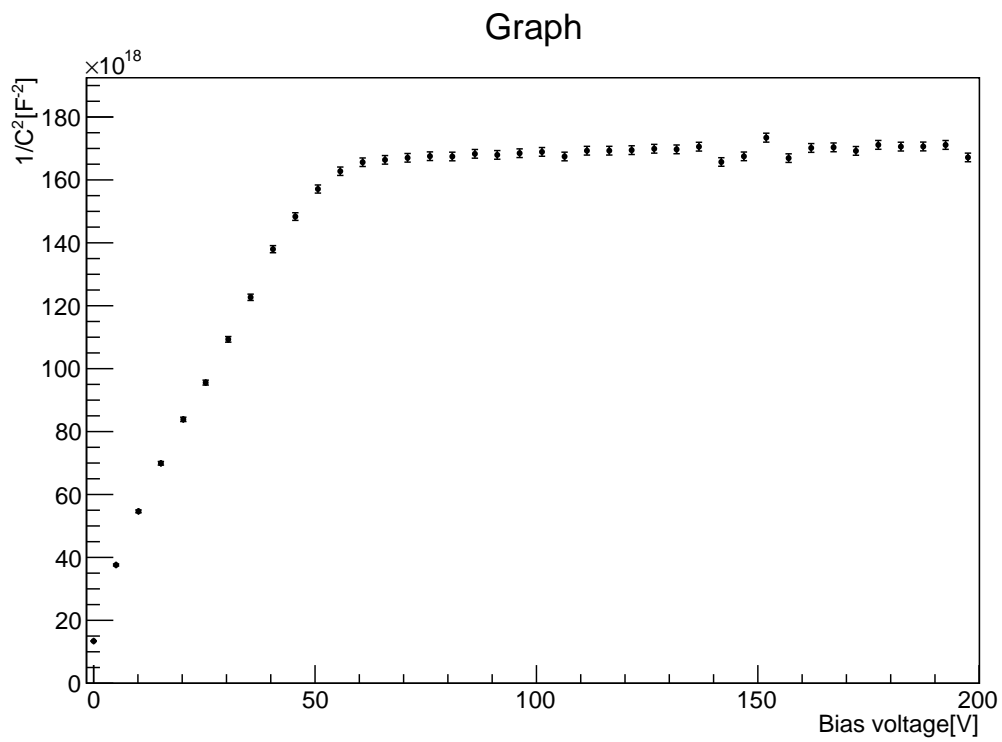


Figure 4.6: Capacitance-voltage plot for baby chip 1-1.

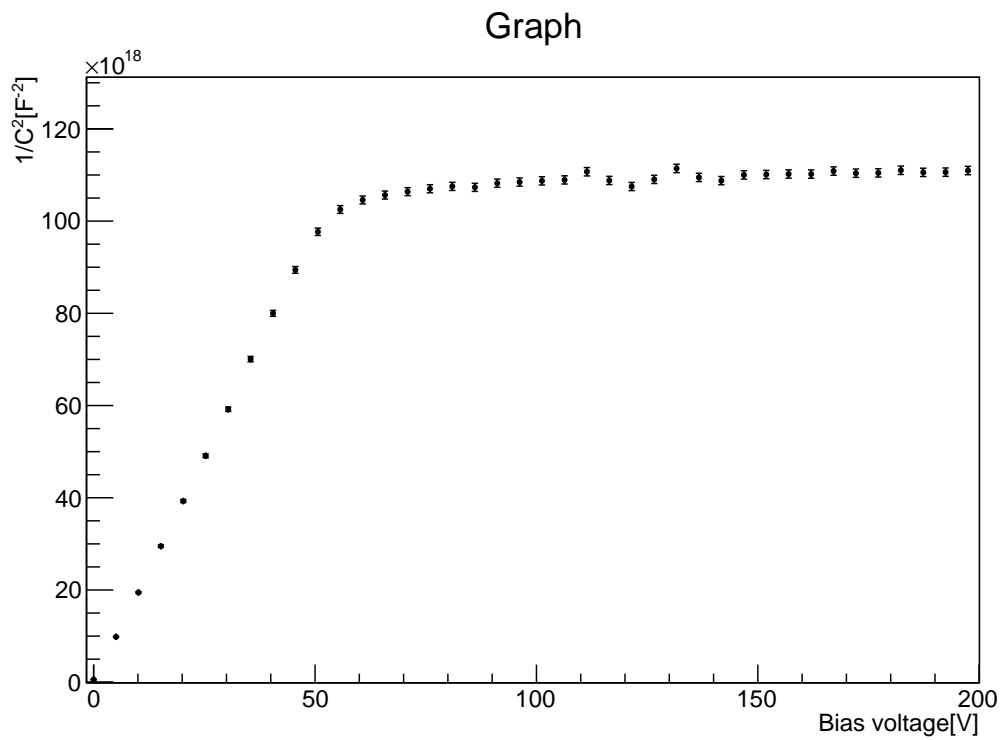


Figure 4.7: Capacitance-voltage plot for baby chip 1-2.

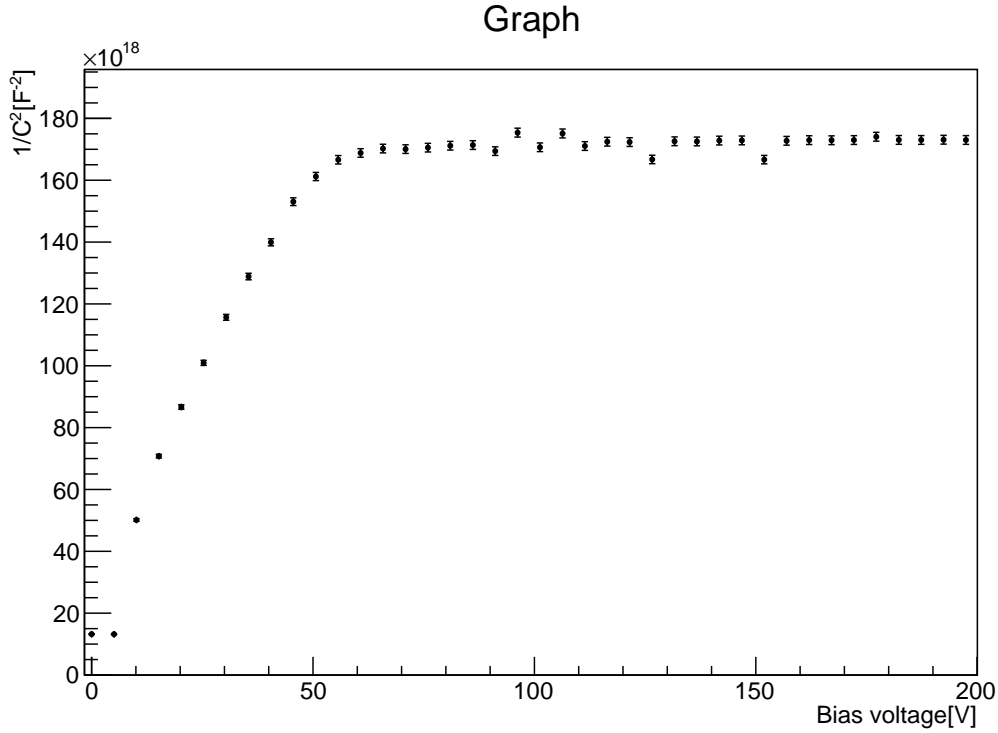


Figure 4.8: Capacitance-voltage plot for baby chip 2-1.

fitted line was used to extract the value of  $\frac{N_A+N_D}{N_A N_D}$ . Because this equation is derived for unit area capacitor, it is rewritten as

$$\frac{N_A + N_D}{N_A N_D} = \frac{1}{2} S q \epsilon_s \epsilon_0 A^2 \quad (4.2)$$

The values are shown in Table 4.1, 4.2. Combined with the measurement of (3.2), this can be used to measure the change in acceptor or donor concentration due to radiation damage.

Table 4.1: The summary of capacitance-voltage measurement results for main chip and baby chip 1-1.

	Main chip	Baby chip 1-1
Saturated capacitance	$2.44 \pm 0.01(\text{stat.}) \pm 0.02(\text{syst.})$ nF	$76.98 \pm 0.09(\text{stat.}) \pm 0.25(\text{syst.})$ pF
Depletion thickness	$335.6 \pm 1.4(\text{stat.}) \pm 2.8(\text{syst.})$ $\mu\text{m}$	$362.51 \pm 0.42(\text{stat.}) \pm 0.42(\text{syst.})$ $\mu\text{m}$
$V_0 = V_D + \frac{q N_A N_D}{2 \epsilon_s \epsilon_0 (N_A + N_D)} d_I^2$	$0.50 \pm 0.16(\text{stat.}) \pm 0.58(\text{syst.})$ V	$8.6 \pm 0.2$ V
$\frac{N_A + N_D}{N_A N_D}$	$1.682 \pm 0.014(\text{stat.}) \pm 0.069(\text{syst.}) \times 10^{-18}$ $\text{m}^3$	$6.336 \pm 0.045 \times 10^{-15}$ $\text{m}^3$

Table 4.2: The summary of capacitance-voltage measurement results for baby chips.

	baby chip 1-2	baby chip 2-1
Saturated capacitance	$95.79 \pm 0.13(\text{stat.}) \pm 0.30(\text{syst.})$ pF	$76.34 \pm 0.11(\text{stat.}) \pm 0.25(\text{syst.})$ pF
Depletion thickness	$291.32 \pm 0.40(\text{stat.}) \pm 0.40(\text{syst.})$ $\mu\text{m}$	$365.55 \pm 0.53(\text{stat.}) \pm 0.53(\text{syst.})$ $\mu\text{m}$
$V_0 = V_D + \frac{qN_A N_D}{2\epsilon_s \epsilon_0 (N_A + N_D)} d_I^2$	$-0.07 \pm 0.05$ V	$6.9 \pm 0.2$ V
$\frac{N_A + N_D}{N_A N_D}$	$4.369 \pm 0.02010^{-15}$ $\text{m}^3$	$6.876 \pm 0.06310^{-15}$ $\text{m}^3$

# Chapter 5

## Charge collection efficiency measurement plan

The charge collection efficiency measurement is described in this section. The charge collection efficiency is expected to decrease after irradiation.

### 5.1 Expected signal voltage

For the measurement of the charge collection efficiency, signals induced by cosmic rays or a radioactive source will be measured. In Sec.2.2.4, the MIP (minimum ionizing particle) signal was estimated to be 0.124 MeV, corresponding to a charge of  $5.45 \times 10^{-15}$  C.

A charge sensitive pre-amplifiers such as the CAEN A1422 will be used to read the signal. This pre-amplifier has a gain of 400 mV/MeV, giving a MIP signal of around 50 mV.

### 5.2 Setup

The setup for signal collection efficiency is shown in Fig.5.1. The measurements of current-voltage and capacitance-voltage properties were shown as the sum of nine pixels. For the signal collection efficiency measurement, each pixel will be measured separately. A printed circuit board will be attached to the silicon sensor with indium, and the read out circuit will be connected to a printed circuit board. A high voltage is required to reverse bias the silicon sensor. Since the pre-amplifier is a charge sensitive amplifier, the peak value of the signal voltage is proportional to the total charge, and therefore the deposited energy. The peak value will be read out by an oscilloscope. There is also a shaper and an ADC read out for digital processing. The signal read out will be triggered by coincident signal from the two scintillator set above and below the silicon sensor.

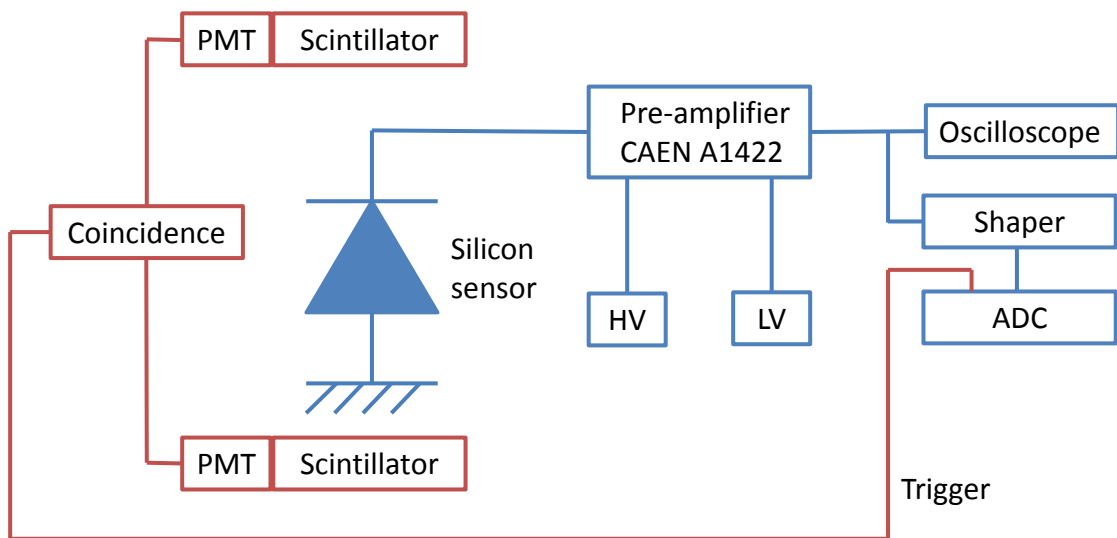


Figure 5.1: The setup for signal collection efficiency measurement.

The signal strength and the pedestal will be measured from the distribution of the measured peak voltages, while the expected signal can be calculated from the energy of the decay product of the radioactive source. The energy resolution will be also measured from the same peak voltage value distribution. There are three major possible contributions to the energy resolution: first, the Poisson distribution due to the number of created e-h pairs, given by  $\sqrt{3.41 \times 10^4}/3.41 \times 10^4 \simeq 0.5\%$  for a MIP signal. For larger energy deposits, it will be smaller; secondly, the noise from the pre-amplifier, estimated to be less than 2 keV according to CAEN A1422H design [11]. It is equivalent to an error of 1.6% for MIP signal; and thirdly, due to the voltage resolution of oscilloscope. An oscilloscope, Tektronix DPO2024 has a sensitivity of 2 mV/div. Therefore, it will contribute an error of 0.4%. In total, the error will be about 1.7 % except environmental noise for MIP signal.

The charge collection efficiency will be measured before and after neutron irradiation to measure the effect of traps and so on.



# Chapter 6

## Simulation of radiation damage effect

In this section, the expected the ILD performance on jet energy reconstruction is discussed. One of the radiation damage effects, noisy pixel is simulated. This discussion gives part of the requirements for radiation hardness of the silicon sensor.

### 6.1 Simulation tools

Events were simulated using the detailed full simulation of the ILD detector using the Mokka [12], GEANT4-based [13] software package. The same detector model as used in the ILD Detailed Baseline Design [2] was simulated. Event reconstruction were performed in the Marlin framework [14]. This includes digitization of the simulated detector signals (including a threshold cut at 0.5 MIP in each ECAL pixel), and reconstruction of events using PFA (see Sec.1.3). For the simulation of the effects of radiation damage, it was assumed that some fraction of pixels is noisy in the ECAL. As a simple, conservative assumption, noisy pixels were assigned an energy of 1.4 MIPs.

If there is no problem in a silicon sensor, the typical signal-to-noise ratio for a MIP is about 10. Therefore, assuming a Gaussian noise distribution, noise larger than the 0.5 MIP threshold is about  $10^{-7}$ . Since there are order of  $10^8$  pixels in total, only around 10 noisy channels will be fired per event. The noise can have 2 effects: add energy to true clusters, increasing event energy; add inducing errors in the clustering or pattern recognition in the ECAL (e.g. making fake clusters, or causing clusters to be merged). If noise hits are isolated, they are not clustered and are essentially ignored in the energy sum.

### 6.2 Result

The jet energy resolution was evaluated using Z boson at rest decaying to two light quarks(u, d, and s). Since the energy resolution is worse in the end-caps, overlapping region of barrel

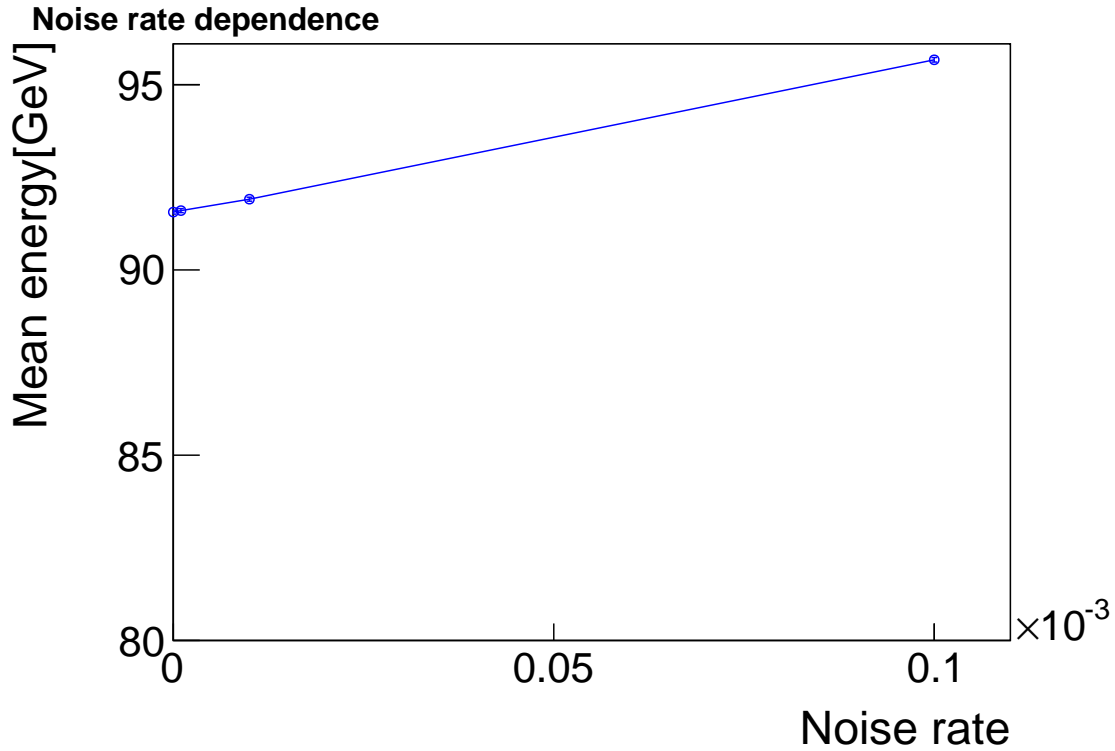


Figure 6.1: The dependence of mean energy on noise rate for  $\sqrt{s} = 91$  GeV jets.

and end-caps, and beam direction, only  $|\cos\theta| < 0.7$  events were used. Here,  $\theta$  is the angle of initial quark direction measured from beam direction. The energy was measured by summing all the reconstructed particle energies. A weak point of the PFA reconstruction is that sometimes mis-clustering occurs [3]. The mis-clustering results in removing a particle from the reconstructed particle list or double counting of same particle. Therefore, only 90% of all the events were used to evaluate the jet energy mean and resolution removing mis-clustering events. These 90% of events were selected to get their reconstructed energy distribution range minimum. RMS90 is defined as the root mean squares of the 90% of the events and interpreted as the energy resolution of the ILD.

Here, the simulation result of  $\sqrt{s} = 91$  GeV jets events with randomly distributed noisy pixels is shown. Fig.6.1 shows the dependence of the mean total reconstructed event energy on the noise rate, showing a linear dependence of the reconstructed energy on the noise rate.

Fig.6.2 shows the dependence of the jet energy resolution on the noise rate. There is no significant effect on the resolution for a noise rate up to  $10^{-5}$  (corresponding to about 1000 noisy pixels per event), while a noise rate of  $10^{-4}$  has significantly degraded jet energy resolution.

Figs.6.3, 6.4 show views of the reconstruction of the same original event, with different noise rates, of  $10^{-5}$  and  $10^{-3}$ , superimposed. In the case of the lower noise rate, no obvious

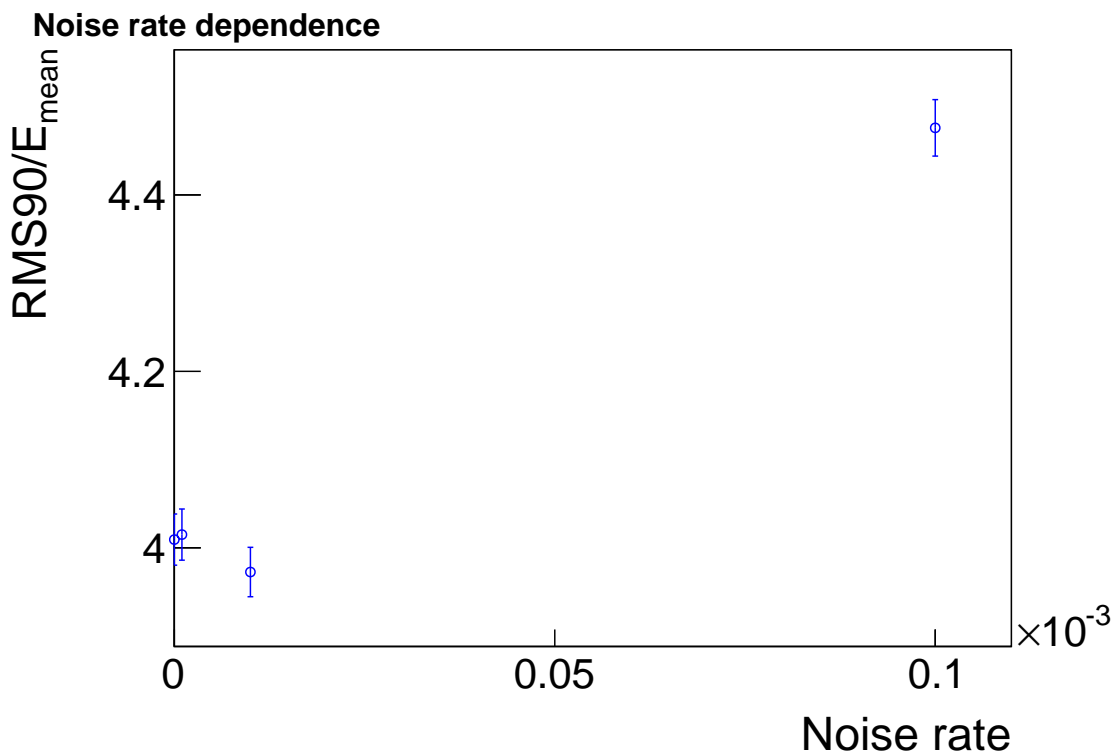


Figure 6.2: The dependence of jet energy resolution on noise rate for  $\sqrt{s} = 91$  GeV jets.

reconstruction problems are visible, while the high noise rate gives rise many fake clusters consisting of noisy pixels.

### 6.3 The requirements on the silicon sensor

In the previous section, it is concluded that the noise rate should be less than around  $10^{-5}$ . In this section, the requirements for the silicon sensor are discussed based on this result. Here, it is assumed that the typical signal to noise ratio is 10 for the silicon sensor before irradiation, and the pedestal has Gaussian distribution with RMS  $\sigma$ . There will be noise rate of  $10^{-5}$  when the threshold is set to  $4.3 \sigma$ .

The requirement for leakage current can be determined because it affects to the pedestal distribution. If the fluctuation of the leakage current increases to get pedestal  $\sigma$  1.2 times larger, it gives noise rate of  $10^{-5}$ .

The requirement for charge collection efficiency can be determined because it decreases the signal threshold and thus increase noisy pixel rate. From the assumed pedestal distribution, the 1 MIP signal should be larger than  $8.3 \sigma$ . Since the 1 MIP signal is  $10 \sigma$  before irradiation, 17% of signal collection efficiency decrease is tolerable. The contribution for the statistics error in MIP signal collection is only 0.1% at the same time, sufficiently small to ignore

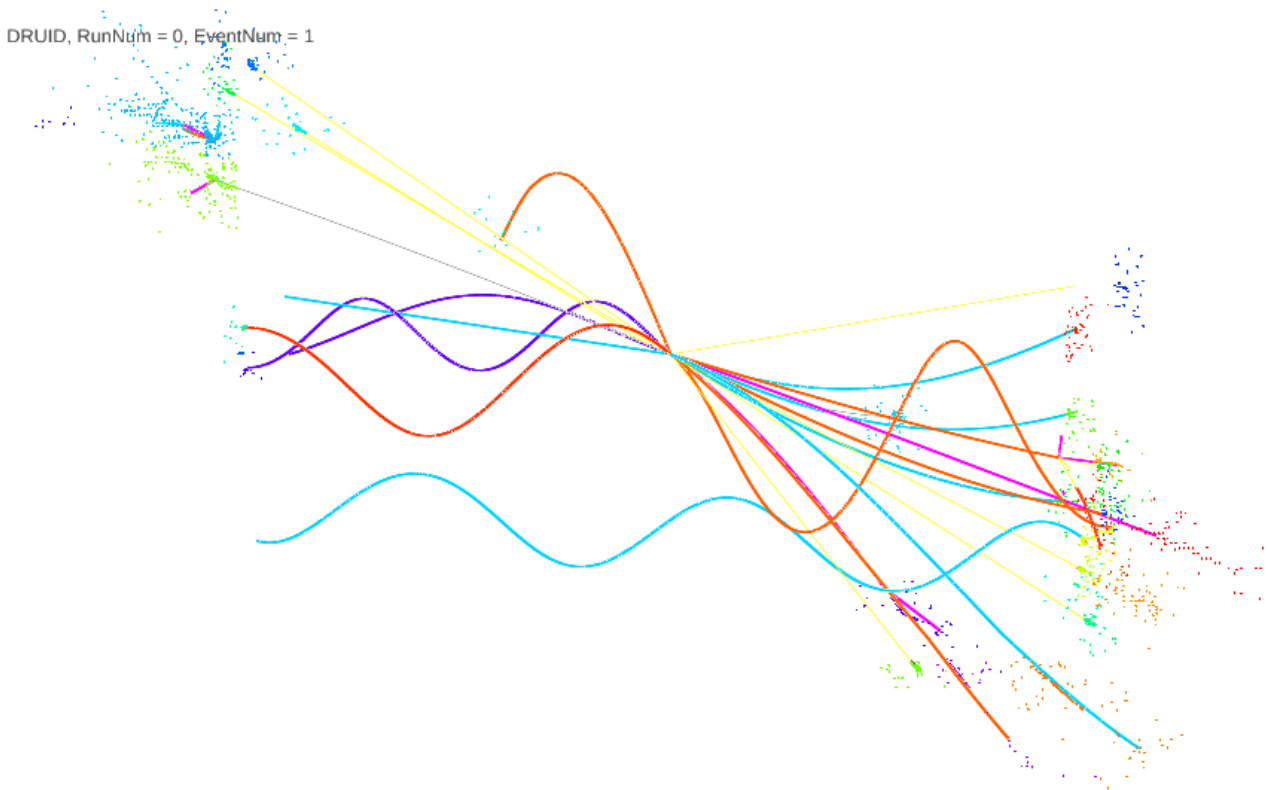


Figure 6.3: One jet event with noise rate of  $10^{-5}$ . The lines are MC particle trajectories, dots are clustered calorimeter hits.

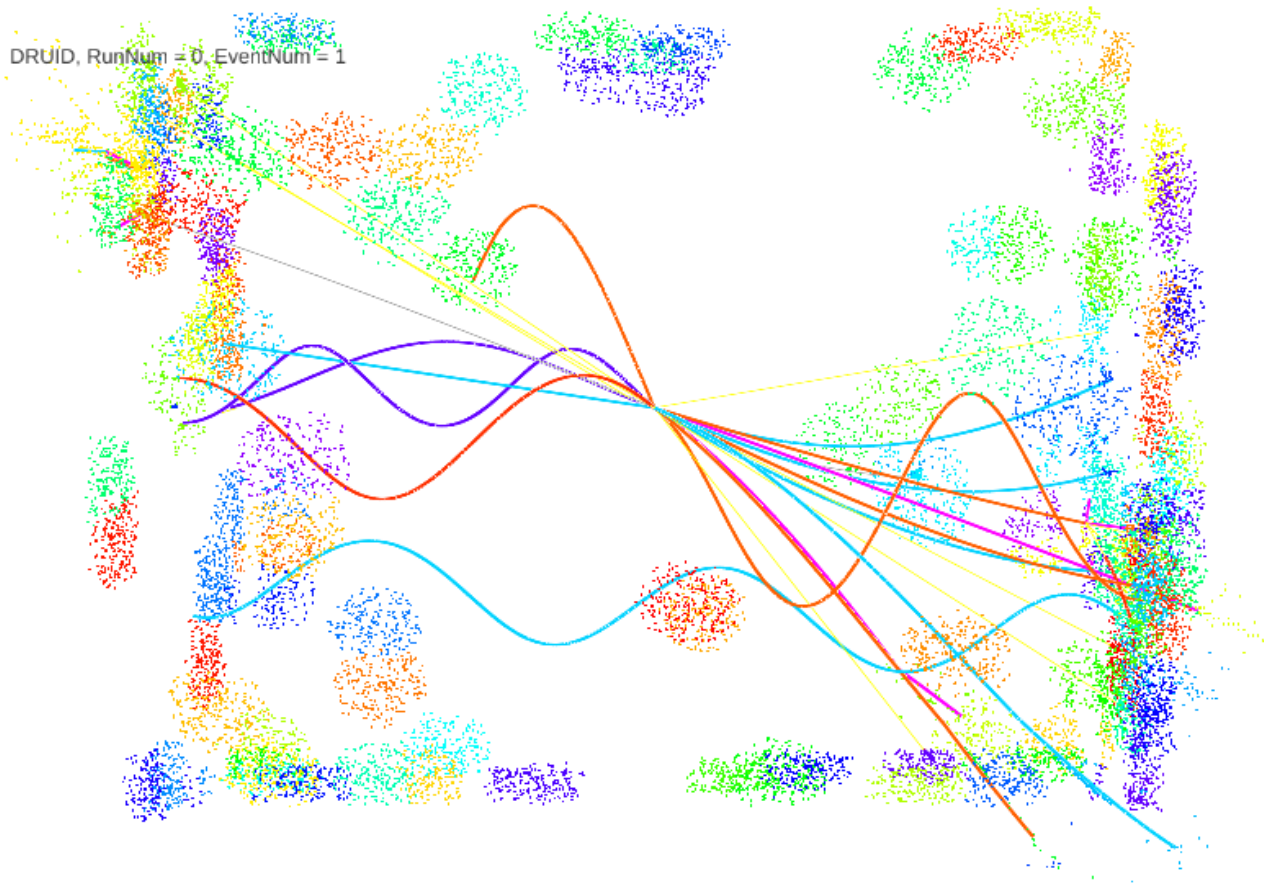


Figure 6.4: One jet event with noise rate of  $10^{-3}$ . The lines are MC particle trajectories, dots are clustered calorimeter hits.

compared to expected MIP signal error 1.7%, discussed in Sec.5.2.

# Chapter 7

## Irradiation experiment plan

### 7.1 Radiation dose

At present, no detailed radiation dose estimate for the ILC ECAL has been performed. However, the expected ECAL radiation dose has been studied in the case of the CLIC [15], and for the ILC neutron dose for the vertex detector from the ILC extraction line beam dump [16]. The CLIC is a future multi-TeV linear collider. The radiation dose in the CLIC should be higher than that in the ILC because it operates with higher centre of mass energy. Therefore, the radiation dose estimation in the CLIC should be conservative for the ILC detector. According to [15], the maximum equivalent neutron flux is  $2 \times 10^{10}$  /cm<sup>2</sup>/year, highest in the forward part of the ECAL end-caps. Equivalent neutron flux is defined by converting total radiation damage to the flux of 1 MeV neutrons which gives the same extent of radiation damage. There are two main source of displacement damage dose, incoherent pairs and  $\gamma\gamma \rightarrow hadron$ . The incoherent pairs include three types of processes,  $\gamma\gamma \rightarrow e^+e^-$  (Breit-Wheeler, BW),  $\gamma e^\pm \rightarrow e^\pm e^+e^-$  (Bethe-Heitler, BH), and  $e^+e^- \rightarrow e^+e^-e^+e^-$  (Landau-Lifshits, LL). The  $\gamma$  is induced by beamstrahlung. The  $\gamma$ s of  $\gamma\gamma \rightarrow hadron$  is also induced by beamstrahlung. There will be  $2 \times 10^3$ /bunch BW events,  $2 \times 10^5$ /bunch BH events, and  $5 \times 10^4$ /bunch LL events in the ILC [17]. While  $\gamma\gamma \rightarrow hadron$  event occurs 3.2 /bunch. The incoherent pair is important because it has larger production angles than coherent pairs. The  $\gamma\gamma \rightarrow hadron$  event number is much smaller, however, the radiation damage is much larger than that of incoherent background. The distribution in the ECAL end-cap is shown in Fig.7.1. The reason there are relatively large dose in deeper layers is that there are backscattering neutrons from the BeamCal located in the very forward region.

As discussed in [16], there are background neutrons not only from the interaction point but also from the extraction line beam dump. The neutron fluence at the interaction point is estimated to be  $4 \times 10^{10}$  n/cm<sup>2</sup>/year 1 MeV equivalent neutrons. It gives larger contribution than beam crossing.

Silicon detector technology has advantage in high granularity multi channel readout.

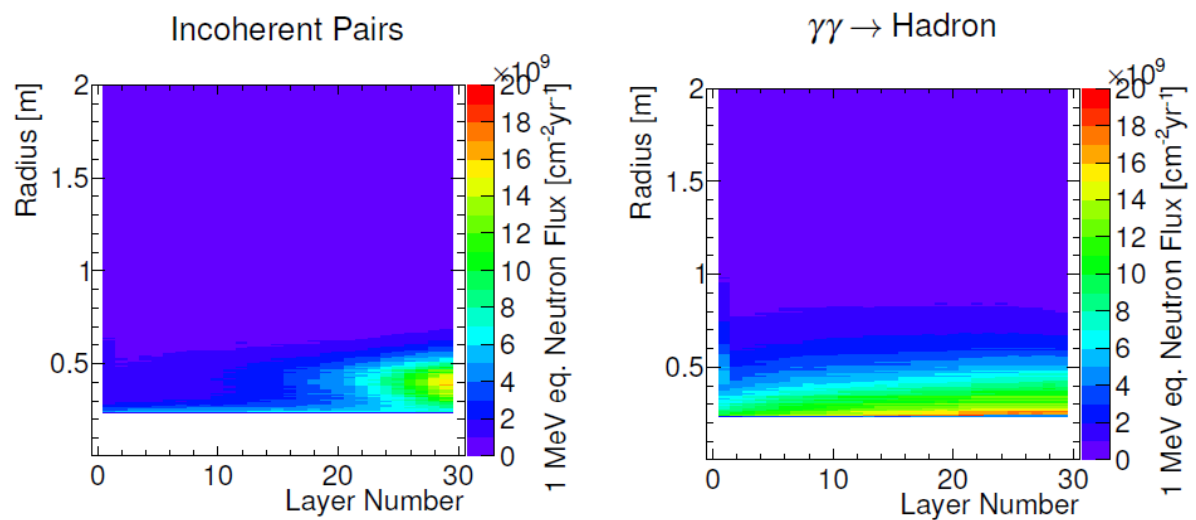


Figure 7.1: 1 MeV equivalent neutron flux distribution in the CLIC-ECAL end-cap. The left is from Incoherent pairs. The right is from  $\gamma\gamma \rightarrow \text{hadron}$ . [15]

Therefore, it will be important technology for the future collider experiments and application in space. For a reference of such a situation, there are  $3 \times 10^{14}$  n/cm<sup>2</sup>/year 1 MeV equivalent neutrons in LHC [18].

## 7.2 Irradiation experiment

The silicon sensor will be irradiated with neutrons in a nuclear reactor at Kyoto University. During irradiation, the silicon sensor will be damaged. Then, it will have some degradation as discussed in Sec.2.3. The damage will be evaluated by comparing measurements of current-voltage, capacitance-voltage, and signal collection efficiency before and after radiation.

In addition, the irradiation test of glue will be performed at the same time. This glue will be used in the ILD ECAL construction to attach the silicon sensor to the printed circuit board.

There are some studies of neutron radiation damage on silicon sensors from other experiments (e.g.[18][19][20]). From past research, it is expected that the silicon sensor will have a decrease of charge collection efficiency of order 0.1% for 5 MeV neutron irradiation of  $10^{12}$  n/cm<sup>2</sup> of neutron irradiation.

As discussed in Sec.7.1, the neutron dose in the ILC will be around  $4 \times 10^{10}$  n/cm<sup>2</sup>/year. However, similar silicon sensors can be used not only in the ILC, but also in other future experiments or in space, where higher neutron backgrounds may be expected. Therefore, a wide range of irradiation tests will be useful. The irradiation test will be done for radiation dose of  $10^{10}$  n/cm<sup>2</sup>,  $10^{12}$  n/cm<sup>2</sup>, and  $10^{14}$  n/cm<sup>2</sup> for with and without glue.



# Chapter 8

## Conclusion

The international linear collider is a planned electron-positron collider operating at centre-of-mass energy between 250 GeV and 1 TeV. The main physics targets at the ILC are the precise measurement of Higgs properties, top quark, W boson, Z boson and new physics such as supersymmetry.

The ILD detector is optimized according to PFA for high resolution, 3-4 % hadronic jet energy measurement. For the electro-magnetic calorimeter, silicon sensors are one options for the detector layers. It is required to be stable for long duration during experiment. Radiation will give some damage to the silicon sensor. To evaluate the radiation damage, a neutron irradiation experiment is planned.

The property of leakage current will be evaluated by current-voltage measurement. Before irradiation, the leakage current was around 10 nA at 120 V, and it was measured with accuracy of a few %. Breakdown voltages are 750 V or not observed up to 800 V. The impurity concentration dependent value  $\frac{I_0}{N_A N_D}$  was measured by a temperature dependence study. The properties of the capacitance-voltage measurement requires more study to improve reliability of measurement system. The charge collection efficiency will be measured soon using radiation source or cosmic ray signal. The neutron irradiation damage can be evaluated by these measurements.

To get the requirement for the silicon sensor, the ILD full simulation study was done with some fraction of noisy pixels. The noise rate of order  $10^{-5}$  is tolerable and it is equivalent to 17% of charge collection efficiency decrease.

The radiation test will be done in a nuclear reactor in Kyoto University. The fluence range of  $10^{10}$  n/cm<sup>2</sup>,  $10^{12}$  n/cm<sup>2</sup>, and  $10^{14}$  n/cm<sup>2</sup> will be tested, corresponding to the ILC operation times of approximately 1 year, 100 year, and the LHC operation time of approximately 1 year, respectively.



# Chapter 9

## Acknowledgements

I would like to show my greatest appreciation to Professor Sachio Komamiya for giving me the chance to research on the ILC detector. I really would like to thank Daniel Jeans. He directed my research wonderfully and is also my good English teacher. Assistant Professor Yoshio Kamiya gave me many helpful advices and warm encouragements. Jacqueline Yan kindly offered feedback on my thesis and is always a brilliant senior student in Komamiya laboratory. I would like to express my gratitude to the CALICE-Asia group members for giving many insightful comments, especially the members of Kyushu University for giving us silicon sensors, measurement box, and tips for the measurement. I have had the support and encouragement of my colleagues, Shion Chen, Maya Okawa, Miki Nishimura, and so on. I would like to thank Kyoko Tanaka, Kuniko Kono, Tomomi Yoshimoto and ICEPP secretaries for supporting me as secretaries.

Last of all, I am deeply grateful to my family support.



# Appendix A

## NIEL

Displacement energy is represented as below with scattering angle  $\theta$ .

$$E_p = E_{p(max)} \sin\left(\frac{\theta}{2}\right) = \frac{2m_0}{M} \frac{1}{m_0 e^2} (E_i + 2m_0 c^2) E_e \sin^2\left(\frac{\theta}{2}\right) \quad (\text{A.1})$$

Here,  $E_i$  is energy of the incident particle,  $c$  is light speed.

In the case of small  $Z$  matter, differential displacement cross section is represented as below using McKinley-Feshbach's equation approximating Mott's solution.

$$d\sigma_p = \frac{4\pi a_0 Z^2 E_R^2}{m_0^2 c^4} \frac{1 - \beta^2}{\beta^4} \left[ 1 - \beta^2 \frac{E_p}{E_{p(max)}} + \pi \alpha \beta Z \left\{ \left( \frac{E_p}{E_{p(max)}} \right)^{1/2} - \frac{E_p}{E_{p(max)}} \right\} \right] \frac{E_{p(max)}}{E_p^2} dE_p \quad (\text{A.2})$$

Here,  $a_0$  is Bohr radius,  $E_R$  is Rydberg energy,  $\beta = v/c$ , and  $\alpha$  is fine structure constant. The displacement cross section can be calculated from integrating (A.2) .

The Lindhard partition factor  $L$  is

$$L = (1 + kg)^{-1} \quad (\text{A.3})$$

$$k = 0.1337 \cdot Z^{1/6} \left( \frac{Z}{A} \right)^{1/2} \quad (\text{A.4})$$

$$g = 3.4008 \epsilon_p^{1/6} + 0.40244 \epsilon_p^{3/4} + \epsilon_p \quad (\text{A.5})$$

$$\epsilon_p = \frac{E_p}{86931 \cdot Z^{7/3}} \quad (\text{A.6})$$

for high energy incident particle.

The NIEL can also be calculated by Monte Carlo method with SRIM (The Stopping and Range of Ions in Matter) code.



# Appendix B

## The Keithley2410 high-voltage source meter specification

The Keithley2410 high-voltage source meter specification is summarized in Tables B.1, B.2.

Table B.1: Keithley2410 high-voltage source meter source specification. [7]

<b>Voltage programming accuracy</b>			
Range	Programme resolution	Accuracy (1 year) 23°C ± 5°C	Noise (peak-peak)
200.00 mV	5μV	0.02% + 600μV	5μV
2.00000 V	50μV	0.02% + 600μV	50μV
20.0000 V	500μV	0.02% + 2.4 mV	5 mV
1000.00 mV	50mV	0.02% + 100 mV	20 mV
<b>Current programming accuracy</b>			
Range	Programme resolution	Accuracy (1 year) 23°C ± 5°C	Noise (peak-peak)
1.00000 μA	50 pA	0.035% + 600 pA	5 pA
10.0000 μA	500 pA	0.033% + 2 nA	50 pA
100.000 μA	5 nA	0.031% + 20 nA	500 pA
1.00000 mA	50 nA	0.034% + 200 nA	5 nA
20.0000 mA	500 nA	0.045% + 4 μA	200 nA
100.000 mA	5 μA	0.066% + 20 μA	1 μA
1.00000 A	50 μA	0.27% + 900 μA	100 μA

Table B.2: Keithley2410 high-voltage source meter measure specification. [7]

<b>Voltage measurement accuracy</b>			
Range	Default resolution	Input resistance	Accuracy (1 year) 23°C ± 5°C
200.00 mV	1 μV	0.012% + 300 μV	>10 GΩ
2.00000 V	10 μV	0.012% + 300 μV	>10 GΩ
20.0000 V	100 μV	0.015% + 1 mV	>10 GΩ
1000.00 mV	10 mV	0.015% + 50 mV	>10 GΩ
<b>Current measurement accuracy</b>			
Range	Default resolution	Voltage burden	Accuracy (1 year) 23°C ± 5°C
1.00000 μA	10 pA	<1 mV	0.029% + 300 pA
10.0000 μA	100 pA	<1 mV	0.027% + 700 pA
100.000 μA	1 nA	<1 mV	0.025% + 6 nA
1.00000 mA	10 nA	<1 mV	0.027% + 60 nA
20.0000 mA	100 nA	<1 mV	0.035% + 1.2 μA
100.000 mA	1 μA	<1 mV	0.055% + 6 μA
1.00000 A	10 μA	<1 mV	0.22% + 570 μA

# Appendix C

## The Agilent LCR meter specification

The Agilent LCR meter specification is summarized in Table C.1.

Table C.1: The Agilent LCR meter specification. [10]

<b>Trigger delay time</b>	
Range	0 s to 999 s
Resolution	100 $\mu$ s (0 s to 100 s) 1 ms (100 s to 999 s)
<b>Step deley time</b>	
Range	0 s - 999 s
Resolution	100 $\mu$ s (0 s to 100 s) 1 ms (100 s to 999 s)
<b>Measurement terminal</b>	four-terminal pair
<b>Test cable length</b>	2 m
<b>Measurement time mode</b>	89 s (medium mode)
<b>Averaging</b>	
Range	1 to 256 measurements
Resolution	1
<b>Test frequency</b>	100 kHz
Resolution	100 Hz
Measurement accuracy	$\pm 0.01\%$
<b>The signal mode</b>	Normal (Program selects voltage or current at the measurement terminals when they are opened or short-circuited, respectively.)
<b>Test signal voltage</b>	20 mVrms
Resolution	100 $\mu$ Vrms
Accuracy	$\pm (10\% + 1 \text{ mVrms})$
<b>The test signal current</b>	
Range	0 Arms to 20 mArms
Resolution	1 $\mu$ Arms (0 mArms to 2 mArms) 2 $\mu$ Arms (2 mArms to 5 mArms) 5 $\mu$ Arms (5 mArms to 10 mArms) 10 $\mu$ Arms (10 mArms to 20 mArms)
<b>Test signal current</b>	
Accuracy	$\pm (10\% + 10\mu\text{Arms})$
<b>Output impedance</b>	100 $\Omega$ (nominal)

# Bibliography

- [1] Ties Behnke et al. (ed.s), "The International Linear Collider Technical Design Report Volume 1. Executive summary", arXiv.1306.6327, (2013)
- [2] Ties Behnke et al. (ed.s), "The International Linear Collider Technical Design Report Volume 4. Detectors", arXiv.1306.6329, (2013)
- [3] M. Thomson, "Particle flow calorimetry and the PandoraPFA Algorithm", Nucl.Instrum.Meth.A611:25-40, (2009)
- [4] A. Kunioka and K. Kamimura, "新版 基礎半導体工学", 朝倉書店, (1996)
- [5] J. Beringer et al. (Particle Data Group), "The review of particle physics", Phys. Rev. D86, 010001 (2012)
- [6] H. Kudo, "原子力教科書 放射線利用", オーム社, (2011)
- [7] Keithley, "Series 2400 SourceMeter instruments", Keithley, (2010)
- [8] W. Bludau, A. Onton, and W. Heinke, "Temperature dependence of the band gap of silicon", Journal of Applied Physics 45, 1846 (1974)
- [9] Agilent Technologies, "インピーダンス測定ハンドブック", Agilent Technologies, (2003)
- [10] Agilent Technologies, "Agilent E4980A プレシジョン LCR メータ ユーザーズ・ガイド", Agilent Technologies,(2013)
- [11] CAEN, "A1422H Lownoise fast rise time charge sensitive preamplifier (Hybrid) Data sheet", CAEN, (2012)
- [12] P. de Freitas, et al., <http://polzope.in2p3.fr:8081/MOKKA>.
- [13] GEANT4 collaboration, S. Agostinelli et al., Nucl. Instr. and Meth. A506 (2003) 3; GEANT4 collaboration, J. Allison et al., IEEE Trans. Nucl. Sci. 53 (2006) 1.
- [14] F. Gaede, Nucl. Instr. and Meth. A559 (2006) 177.

- [15] A. Sailer, "Saturation and Radiation Doses in the ECAL", CLIC Detector and Physics Meeting, [http://indico.cern.ch/getFile.py/access?contribId=12&sessionId=8&resId=0&materialId=slides &confId=267137](http://indico.cern.ch/getFile.py/access?contribId=12&sessionId=8&resId=0&materialId=slides&confId=267137) (2013)
- [16] S. Darbha, "Simulation of Neutron Backgrounds from the ILC Extraction Line Beam Dump", SLAC-TN-07-013, (2007)
- [17] K. Yokoya and Pisin Chen, "BEAM-BEAM PHENOMENA IN LINEAR COLLIDERS", KEK preprint, (1991)
- [18] G. Lindström, "Radiation damage in silicon detectors", Nucl.Instrum.Meth. A 512, (2003) 30-43
- [19] E.Fretwurst, H.Herden, G. Lindström, U.Pein, M. Rollwagen, H. Schatz, P. Thomsen and R. Wunstorf, "Silicon detector developements for calorimetry: technology and radiation damage", Nucl.Instrum.Meth. A288, (1990) 1-12
- [20] R. Wunstorf, M. Benkert, E.Fretwurst, G. Lindström, T.Schulz, N.Croitoru, R. Darvas, M. Mudrik, R. Böttger, and H. Schölermann, "Radiation damage of silicon detectors by monoenergetic neutrons and electrons", Nuclear physics B 23A, (1991) 324-332